Evidence of the Nonstationarity of the Terrestrial Bow Shock from Multi-Spacecraft Observations: Methodology, Results and Quantitative Comparison with PIC Simulations

5 Christian Mazelle[1] and Bertrand Lembège[2]

[1]IRAP, CNRS, University of Toulouse, UPS, CNES, Toulouse, 31400, France.
[2]LATMOS, CNRS, University of Velizy Saint-Quentin, Guyancourt, 78390, France.

Correspondence to: Christian Mazelle (cmazelle@irap.omp.eu)

Abstract. The nonstationarity of the terrestrial bow shock is analyzed in detail from in situ magnetic field measurements

10 issued from the FGM experiment on board of Cluster mission. Attention is focused on statistical analysis of quasiperpendicular supercritical shock crossings. The present analysis stresses for the first time the importance of a careful and accurate methodology in the data processing which can be a source of confusion / misunderstanding if not treated properly. The analysis performed using 96 shock front crossings shows evidence of a strong variability of the microstructures of the shock front (foot and ramp) which are analyzed in deep details. Main results are : (i) most statistics clearly evidence that the ramp thickness is

15 very narrow and can be as low as a few c/ω_{pe} (electron inertia length), (ii) the width is narrower when the angle θ_{Bn} (between the shock normal and the upstream magnetic field) approaches 90°, (iii) the foot thickness strongly varies but its variation has an upper limit provided by theoretical estimates given in previous studies (e.g., Schwartz et al., 1983; Gosling and Thomsen, 1985; Gosling and Robson, 1985); (iv) the presence of foot and overshoot, as shown in all front profiles confirms the importance of dissipative effects. Present results indicate that these features can be signatures of the shock front self-

20 reformation among a few mechanisms of nonstationarity identified from numerical simulation/theoretical works.

A comparison 2D PIC simulation for a perpendicular supercritical shock (used as reference), has been performed and it shows that: (a) the ramp thickness varies only slightly in time over a large fraction of the reformation cycle and reaches a lower bound value of the order of a few electron inertial length, (ii) in contrast, the foot width strongly varies during a self-reformation cycle but always stays lower than an upper bound value in agreement with the value given by Woods (1971), and (iii) as a

25 consequence, the time variability of the whole shock front is depending on both ramp and foot variations.

Moreover, a detailed comparative analysis shows that much elements of analysis were missing in previous reported works concerning both (i) the important criteria used in the data selection and (ii) the different and careful steps of the methodology used in the data processing itself. This absence of these precise elements of analysis makes the comparison with present work difficult, worse, it makes some final results and conclusive statements quite questionable at present time. A least, looking for

30 a precise estimate of the shock transition thickness presents nowadays a restricted interest, since recent results show that the terrestrial shock is rather nonstationary and one unique typical spatial scaling of the microstructures of the front (ramp, foot)

must be replaced by some 'variation ranges' (with lower bound/upper bound values) within which the spatial scales of the fine structures can extend.

35 *Copyright statement.* 2020 IRAP France, All rights reserved

1 Introduction

Collisionless shocks are of important interest in space physics, plasma physics and astrophysics. These are commonly believed to be important sources regions of very energetic particles. The analysis of the shock front fine structures is a key question since it specifies the processes of particles energization that are taking place locally. One major difficulty lies on the fact that

40   different processes take place over different spatial ranges and time scales and may interact one with each other.

One can distinguish three main development stages in the front structure studies: first, early attempts to determine shock scale were performed by Holzer et al. (1966) from the magnetic field measurements issued from OGO-A satellite. The technic used at that time was applied to data of EXPLORER 12 (Kaufmann, 1967) and OGO-1 spacecraft (Heppner et al., 1967). Despite the strong assumptions used, shock velocity estimates of ~ 10 km/sec were obtained in agreement with some later

45   measurements (e.g., Balikhin et al., 1995). An improved approach has been performed by using two "almost" simultaneous crossings of the shock front by OGO-5 and HEOS-1 spacecraft (at that time we were still before the launch of the ISEE mission) which were quite distant one from each other (Greenstadt et al., 1975). The shock velocity has been estimated assuming that the shock surface is planar (no front rippling). This assumption was scrutinized during the shock crossings by Greenstadt et al. (1972, 1975). However, this method cannot apply to a large number of shock crossings because the probability

50   that two different spacecraft remains close to each other and cross the same bow shock almost simultaneously is quite low. However, both technics produce values of the laminar shock thickness (i.e. identified later as subcritical shocks), in agreement with later measurements by ISEE spacecraft (Russell et al., 1982).

Second, the works on dual-spacecraft missions such as ISEE 1 & 2 and later AMPTE- UKS considerably improved our knowledge of shock structures and classification (e.g., quasi-perpendicular/parallel and subcritical /supercritical shocks). At

55   that time, even though significant efforts had been focused on quantifying the thickness of subcritical shock fronts with different methods, a major difficulty still persisted. According to different theories, the shock thickness seems to be similar (Balikhin et al., 1995). The large number of reliable shock velocity and thickness estimates from dual-spacecraft studies, with small inter-spacecraft separation, allowed to overcome this difficulty (Russell et al., 1982). However, statistics from multi-spacecraft studies have shown that subcritical shocks are relatively rare, i.e., the terrestrial bow shock is typically supercritical

60   (Balikhin et al., 1995). Profiles of supercritical shocks are more complex than for subcritical ones. Other methods have been proposed to estimate the widths of the microstructures (ramp, foot, overshoot) identified within the front of a supercritical shock. ISEE 1 & 2 observations have strongly stimulated the analysis of their spatial thickness (Livesey et al., 1982; 1984; Gosling and Thomsen, 1985; Mellott and Livesey, 1987; Scudder et al., 1986). However, at that time, the vision of most works

was mainly based on a stationary terrestrial bow shock, and the scaling was referring the thickness of the whole shock front
65   (and not its microstructures) and this thickness has been expressed in terms of the ion inertial length scale.

Third, an improved approach has been supported by the quadri-satellite Cluster mission which not only allowed to analyze
in great details the fine structures within the shock front itself, but also clearly evidenced that the terrestrial bow shock can be
strongly nonstationary (Horbury et al., 2001, 2002; Walker at al., 1999; Moullard et al., 2006; Mazelle et al., 2010; Lobzin et
al. 2007; Lefebvre et al., 2009; Meziane et al., 2014, 2015). More generally, the nonstationarity of quasi-perpendicular shocks
70   in a supercritical regime has been also evidenced in plasma laboratory experiments several decades ago (Morse et al., 1972),
and largely analyzed in numerical simulations (Biskamp and Welter, 1972; Forslund et al., 1984; Lembège and Dawson, 1987;
Winske and Quest, 1988; Lembège and Savoini, 1992; Lembège et al., 2008, 2009; Nishimura et al., 2003; Schöler and
Matsukiyo, 2004; Chapman et al., 2005). Particle-in-cell (PIC) and hybrid simulations clearly evidenced different processes
as sources of the shock front nonstationarity which are summarized as follows (Lembège and al., 2004):

75   a) the self-reformation driven by the accumulation of the reflected ions at a foot distance from the ramp. During their
coherent gyromotion, the reflected ions accumulate at roughly the same location and build up a foot whose amplitude largely
increases in time until its upstream edge suffers an important steepening and becomes a new ramp. New incoming ions are
reflected at this new ramp and the same process continues cyclically. This process has been shown to be quite robust since it
was evidenced in hybrid and PIC simulations as well as in 1D (Biskamp and Welter, 1972; Lembège and Dawson, 1987;
80   Lembège and Savoini, 1992; Hada et al., 2003; Schöler et al., 2003; Schöler and Matsukiyo, 2004), in 2D (Lembège and
Savoini, 1992), and 3D PIC simulations (Shinohara et al., 2007). The self-reformation persists for oblique propagation and
disappears (i) when the oblique direction of the shock front normal is below a critical angle for which the density of newly
reflected ions is too weak to feed the ions accumulation (Lembège and Savoini, 1992), and (ii) for shocks with higher β_i (the
ratio between thermal ion pressure and magnetic pressure) (see Sect. 5.1) as shown by Schmitz et al. (2002) and Hada et al.
85   (2003), or equivalently as the ratio v_{sh}/v_{thi}, where v_{sh} is the shock velocity in the solar wind rest frame and v_{thi} is the upstream
ion thermal velocity (solar wind protons), is relatively weak (a few units) (Schöler et. al., 2003).

b) a similar self-reformation is also observed in 1D PIC simulation of an oblique propagating shock (in a configuration
not exactly perpendicular) but has a different origin since it is mainly driven by a microinstability (MTSI or Modified Two
Stream Instability) excited by the relative drift between incoming electrons/incoming ions within the foot region. This
90   instability develops quickly enough to thermalize the ions and generates a pressure increase which contributes to the build-up
of a new ramp (Matsukyio and Schöler 2003; Schöler and Matsukiyo, 2004). In addition to low β_i, high/realistic mass ratio
and a slightly oblique propagation are necessary conditions (small but finite component of wave vector parallel to the ambient
magnetic field) for the MTSI to be excited.

c) the so-called gradient catastrophe process (Krasnoselskikh et al., 2002) which results only from an imbalance between
95   nonlinear and dispersive effects (Galeev et al., 1999), is expected as the Alfven Mach number M_A is above a critical threshold
(or equivalently the shock front propagation is below a critical value). When this condition is satisfied, large amplitude
nonlinear whistler waves are emitted from the ramp and are responsible for the front nonstationarity. This process also requires

a slightly oblique propagation necessary for the emission of these nonlinear whistler waves. However, this theoretical process has very strong constraints as it is based on 1D model only and excludes any dissipative effect. Indeed, reflected ions (which play a key role in supercritical Mach regime) are neglected and their impact on the shock dynamics is totally absent.

d) the emission of large amplitude whistler waves within the front which propagate obliquely both to the shock normal direction and to the static magnetic field; this mechanism has initially been evidenced for a perpendicular shock (Hellinger et al., 2007; Lembège et al., 2009), and later for a quasi-perpendicular shock by Yuan et al. (2009). It is basically a 2D mechanism, which has been retrieved both in 2D-hybrid and 2D-PIC simulations and has been observed in 3D PIC simulation (Shinohara et al., 2007). One expects that the presence of these waves within the front enlarges the width of the ramp (since these propagate almost at the same velocity of the shock front), but no detailed measurement has been reported yet. One proposed mechanism could be the ion Weibel instability triggered by the reflected gyrating ions (Burgess et al., 2016). Up to now, the mechanism responsible for this wave emission has not been clearly identified yet.

This paper represents an extensive and more detailed analysis of previous works (Mazelle et al., 2007, 2008a, 2008b, 2010a, 2010b, 2011, 2012). Its aim is motivated by the following questions: (i) what important cautions are necessary when measuring carefully the spatial widths of the fine structures (foot and ramp) of the shock front from experimental data? (ii) what are the sources of confusion or misunderstanding when comparing the present results (based on statistics of shock crossings) with interpretations of experimental data made in previous analysis mainly based on one or a few shock crossings only ?, (iii) among the different mechanisms proposed as sources of the shock front nonstationary is it possible to extract some features from the shock front microstructures (observed in experimental data) allowing to clearly identify the dominant nonstationary processes?

The paper is organized as follows. Section 2 presents the motivation, data selection and methodology. A detailed analysis of individual shock crossings is presented in Sect. 3. The results of a statistical analysis and the comparison with PIC numerical simulations results are reported in Sect. 4. Section 5 is devoted to the comparison with previous studies (both experimental and numerical) while Sect. 6 draws some conclusions.

2 Motivation, data selection and methodology

2.1 Experimental data

The constraint on time resolution necessitates the sole use of the magnetic field data for the present detailed analysis. Particle data will be used only to provide the necessary "contextual" plasma parameters, since their time resolution is commonly much lower than the magnetic field data. The latter are provided by the fluxgate magnetometer (FGM) (Balogh et al., 2001). Since the thicknesses of the shock front micro-structures must be determined accurately, the use of the best time resolution is vital, i.e., 22 Hz to 66 Hz depending on the available telemetry. But, lower time-resolution data (5 Hz and 1 Hz) are also used for comparison and to confirm the temporal extension of shock front micro-structures (mainly the ramp and the magnetic foot; the

overshoot/undershoot are not analyzed in detail herein) when the level of microturbulence is relatively high. This is also very
130   important for validating the determination of the shock normal vector (see Sect. 2.2).

Using the appropriate data from both Cluster and ACE satellites, the major shock parameters have been derived: the
Alfvenic and magnetosonic Mach numbers M_A and M_{MS}, the angle θ_{Bn} between the upstream interplanetary magnetic field and
the local shock normal, and the ion β_i. We use herein Cluster particle data used from the Cluster Ion Spectrometer (CIS)
experiment which is extensively described in Rème et al. (2001). It consists of two sensors: (i) a Hot Ion Analyzer (HIA)
135   measuring particles within the energy range 0.005–26 keV, and (ii) a time-of-flight mass spectrometer (CODIF), combining a
top-hat analyzer with a time-of-flight section to measure the major species H+, He+, He++ and O+ covering an energy range
extending from 0.02 to 38 keV/q. Both instruments allow to measure full 3D distributions with a typical angular resolution of
22.5°×22.5° within one satellite spin period (4 s). Two operational modes are possible: in "normal" telemetry modes, one
distribution is transmitted every two or three spins (depending on the time of measurements), whereas in "burst" telemetry
140   modes the distribution is transmitted at every single spin. With the instrumental characteristics mentioned above, both the solar
wind plasma and the energetic particles are detected. The measurements of the HIA analyzer are performed with high geometry
factor (HIA-G) suitable for upstream ion measurements as well as with low geometry factor (HIA-g) suitable for the solar
wind plasma measurements which use specific narrower angular bins (5.6°x5.6°). We are primarily interested in the moments
of the velocity distribution obtained from both 'solar wind' modes and 'magnetospheric' modes of the HIA instrument. The
145   best determination of the upstream solar wind parameters (density, velocity, and temperature) is obtained for a 'solar wind'
mode where HIA-g data are available. For a 'magnetospheric' mode, the solar wind velocity is still correctly determined though
less accurately than in a 'solar wind' mode; however, the density is often underestimated, and the temperature is overestimated
by a large factor when compared to other data sets (for details, see Rème et al., (2001)). The density underestimate is due to a
saturation effect for the solar wind beam while the temperature overestimate is due to the use of wide angular bins of the High-
150   G part of the HIA instrument. In this case, we use ACE satellite data considering the proper time-shift between ACE and the
Cluster constellation.

Figure 1 displays a typical example of a quasi-perpendicular shock crossed by the Cluster spacecrafts. The top panels
show the profiles of the magnetic field magnitude measured by FGM at the spin time resolution (4s-average). The profiles
seem very similar at first glance and do not allow any precise determination. In contrast, the bottom panels show the same
155   shock crossing with high time resolution data. Many differences are then clearly revealed, which illustrate the necessity to use
the best possible time resolution. The methodology used here needs a relatively small separation distance between all four
satellites in term of ion inertial length. This was the case only during the spring seasons of 2001 and 2002 for which all the
inter-distances lied between 100 to 600 km typically, which is no more the case for more recent satellite configurations
(Escoubet et al., 2015). Moreover, the Earth's bow shock is often crossed many times by the four satellites in this configuration
160   as the quartet remains nearby the shock front itself while the shock is globally moving inward and outward.
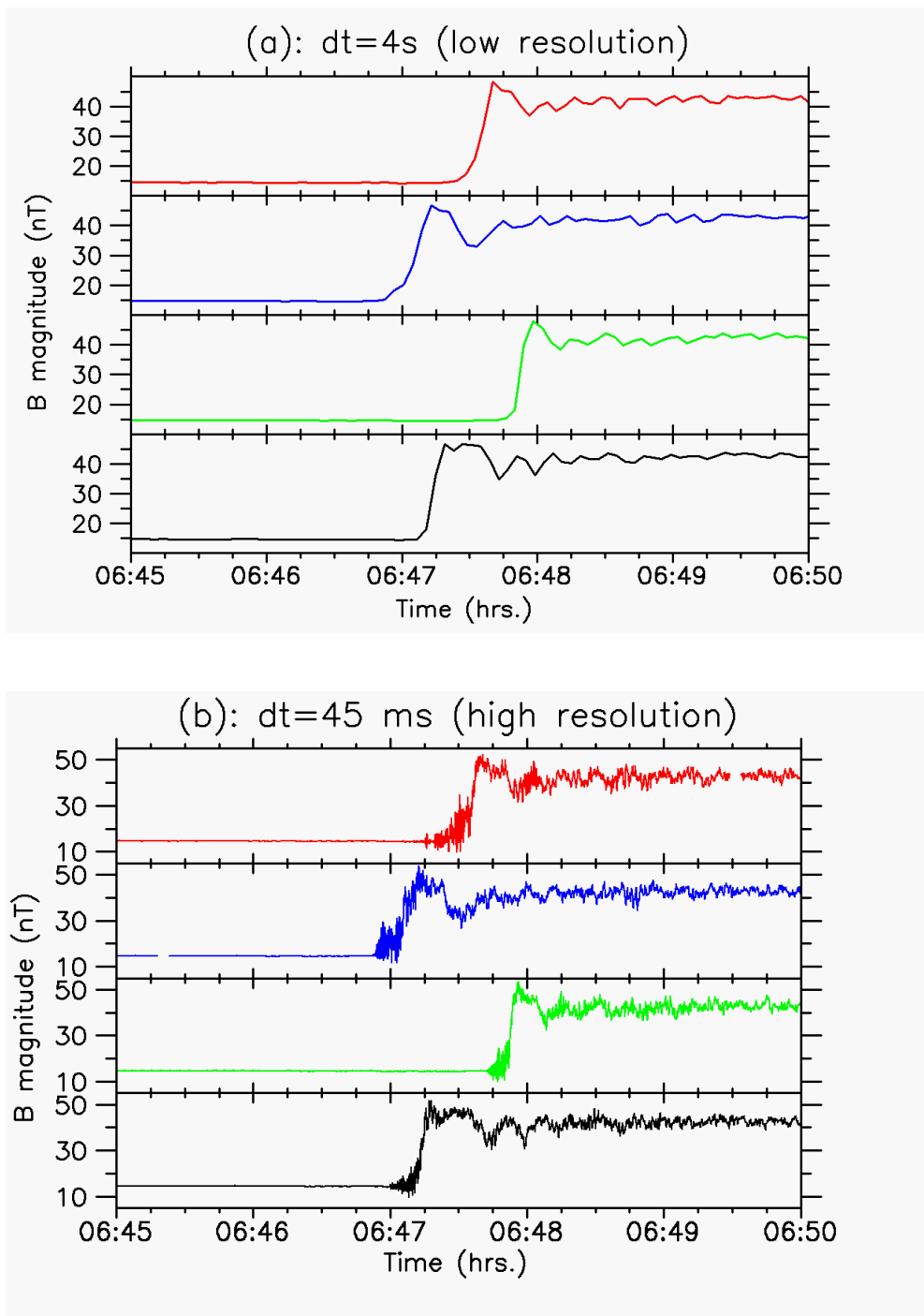
Figure 1. Total magnetic field amplitude measured versus time during the same shock crossing by each of the 4 Cluster satellites on 04/22/2001 around 0647 UT ($M_A = 3.8$; $\beta_i = 0.04$ so that $v_{sh}/v_{thi} \gg 1$, $\theta_{Bn} = 89°$). The same measurement is performed at low time resolution (dt=4s in panel (a)) and high time resolution (dt= 45 ms in panel (b)).

165

2.2 Methodology

We detail for the first time a new methodology to carefully analyse experimental data for the study of super-critical quasi-perpendicular shocks. The step-by-step analysis method we have developed is illustrated on Figure 2 and is conceptually straightforward. First, for each satellite, the temporal extension of each micro-structure of the shock front is determined in the

170   time series of the magnetic field. For each of them, beginning and end times are first estimated by visual inspection. For many previous studies in the literature, the process usually stops at this level leaving the possibility of strong bias. Here, this first step is made only to initialize later automatic algorithms which will be used eventually to get spatial error bars (both for the outer and inner edge of each micro-structure). For each beginning or end time of a micro-structure, we get a first estimate of an error bar on it by defining two associated times: one time (e.g. t_a) when the spacecraft has already likely entered the shock

175   front or left the previously estimated substructure; a second time (e.g. t_b) is defined as when the spacecraft is inside the present substructure for sure. The order of these two times obviously depends whether there is an inbound or outbound bow shock crossing. This may appear arbitrary and occasionally difficult to estimate but the experience shows that the risk to miss the real beginning/end time inside the defined interval is low.

        The determination of upstream parameters entails a steady asymptotic upstream interplanetary magnetic field (IMF) $\underline{\mathbf{B}}_0$

180   associated with each shock crossing by the four spacecraft. For highly perpendicular shocks, it is however often possible to define an unperturbed upstream field on a time scale around a few minutes. For each satellite, we must define an upstream time interval displaying a magnetic field quite steady both in components and magnitude. For each spacecraft s/c_i, where s/c_i holds for **s**pace**c**raft "i" among the Cluster quartet (where $i = 1, 4$), an average upstream field $\underline{\mathbf{B}}_{0i}$ is computed. Its magnitude is shown in the lower green horizontal line in Figure 2a for one example of a single spacecraft shock crossing. Again, an initial

185   estimated time interval is obtained from the visual inspection of the time series. The time duration cannot be too long since the usual stability time scale of the IMF due to the intrinsic solar wind variability (turbulence and directional discontinuities) is rarely more than a few tens of minutes (*e.g.,* Burlaga, 1971) which we can take as an upper limit Δt_u. In order to be physically reliable, Δt_u cannot be too short. One reasonable lower limit Δt_l is the time interval during which a solar wind parcel travels a distance of one ion inertial length (about 100 km usually) that is about one minute typically, considering the mean spacecraft

190   velocities are all consistent within a reasonable range. In this purpose, the six relative angles θ_{ij} measured between upstream fields $\underline{\mathbf{B}}_{0i}$ and $\underline{\mathbf{B}}_{0j}$ for s/c_i and s/c_j with ($i,j = 1$ to 4) are computed. The upstream vector $\underline{\mathbf{B}}_{0i}$ measured by satellite "i" must be as possible close to the vector $\underline{\mathbf{B}}_{0j}$ measured by another satellite "j". If all angles θ_{ij} are less than $5°$ (arbitrary value chosen herein from empirical considerations), then the procedure is pursued, otherwise, the upstream time intervals (where these θ_{ij} values are calculated) are automatically modified by slightly shifting and reducing them until the above constraint on θ_{ij} is satisfied.

195   The shock event is rejected from the present analysis when the adjustment fails or not satisfactory.

        When possible, the use of a larger time interval improves the statistics. Using the initial estimate of Δt and constraining it to be between Δt_l and Δt_u, the finest upstream interval corresponds to the lowest values of the standard deviations σ for both the magnitude and components of the field. Though this can be easily verified by visual inspection, it allows to ensure the

absence of any solar wind disturbance. The following step deals with the determination of a unique unperturbed ambient IMF

200    $\underline{\mathbf{B}_0}$ for every shock crossing by the four-spacecraft constellation. First, it is necessary to compare the individual upstream fields $\underline{\mathbf{B}_{0i}}$. This determination of $\underline{\mathbf{B}_0}$ is of crucial importance for the present study since it impacts both the value of the shock Alfven Mach number through the field magnitude used and the determination of the angle θ_{Bn0} between $\underline{\mathbf{B}_0}$ and the global shock normal $\underline{\mathbf{n}_0}$. This is obviously the first possible source of error in the determination of both the upstream Alfven velocity, the Alfven and magnetosonic Mach numbers and the angle θ_{Bn0}.

205   For each satellite, the standard deviations σ obtained above for the magnetic field components and magnitude allow the determination of the time when the spacecraft penetrates inside the magnetic foot. We determine, for each component and magnitude, the time when it is above 3-σ threshold level and close to the initially estimated time of the entry in the foot obtained by visual inspection (t_a blue dashed line in Figure 2a). Then, we select the 'external' limit of this entry (t_1 in Figure 2a) among these four times as the closest to the external estimate t_a and the 'internal limit' (t_2 in Figure 2a) as the closest to

210   the estimated internal estimate (t_b blue dashed line in Figure 2a). The derived times t_1 and t_2 then define the error bar of the foot entry in the time domain. For the present case, the visual estimate t_b nearly coincides with the time t_2 automatically determined. Moreover, the possible presence of solar wind or foreshock transients as well as detached whistler wave packet must be avoided. The later occurs quite often even in the nearly perpendicular configuration and can easily leads to a wrong determination. Also, solar wind transients are always possible while foreshock transients may only be an issue for more

215   'oblique' configuration which is not addressed in the present study. Nevertheless, it is necessary to make a cautious post visual inspection.

          Similarly, the initial estimated times of the other substructures are labelled with letters and the final times determined from the present methodology are labelled with numbers. The times t_c and t_d are the initial 'visual' estimates for the exit from the foot and entry in the ramp respectively. They will be only used for initializing the automated algorithm described below.

220   A major caveat in many previous attempts to compute the ramp thickness in the literature is to include in the ramp the part of the magnetic field profile up to the maximum of the first overshoot. To avoid that and to well define at least the first overshoot we need to determine a downstream (asymptotic) level which would be required for instance for checking the Rankine-Hugoniot conditions. For that purpose, it is necessary to define a downstream interval in the magnetosheath far enough from the consecutive overshoots/undershoots displaying a quasi-steady magnetic field. This choice is highly important and not

225   always straightforward in the case of very close consecutive crossings (multiple crossings) where only an average over the region of the sequence of overshoots / undershoots will be estimated. When a "clean" time interval downstream from this overshoots / undershoots interval is available, the average values obtained for B magnitude and components can be compared to the values inside the overshoots/undershoots interval. If these values are in good agreement, the downstream interval is appropriate for the determination of the asymptotic value. When a "clean" time interval downstream from this

230   overshoots/undershoots interval is available, the average values obtained for B magnitude and components can be compared

to the values inside the overshoots/undershoots interval. If these values are in good agreement, the downstream interval is appropriate for the determination of the asymptotic value. It is then used to give an initial estimate (te, tf) of the final time
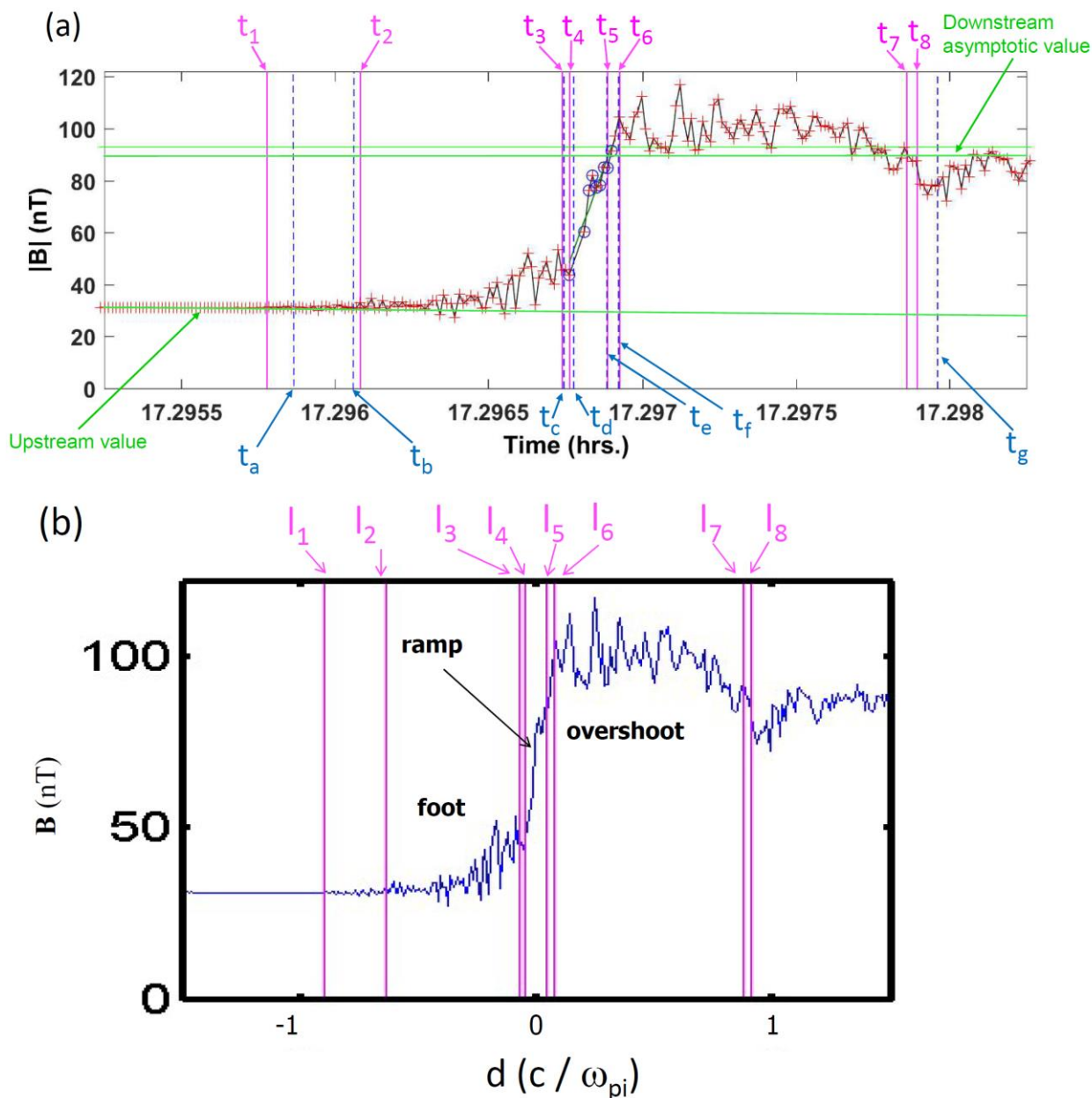
Figure 2: (a) Temporal profile of the magnetic field magnitude B for one satellite crossing only (measured by one of the Cluster satellites C1 on 03/31/2001 around 1717:50 UT; times are shown as decimal hours). The individual data points are shown as red crosses; the green horizontal lines indicate the asymptotic upstream B_0 and downstream B_d +/-5% B_d values. The initial time estimates are labelled with letters (t_a to t_g) and the final times determined from the automatic methodology are labelled with numbers (t_1 to t_8); (b) Corresponding spatial profile along the shock normal for the same B-field magnitude obtained from the time series of Figure 2a; the locations labelled with numbers (l_1 to l_8) have been deduced from the final times (t_1 to t_8) from panel (a). Adapted from Mazelle et al. (2010).

interval (t_5, t_6) for the exit from the ramp/entry in the overshoot by using +/- 5% of the computed asymptotic value (which is arbitrary but appears to be a good empirical compromise). It should be mentioned that a 1-σ level can also be determined here but it will usually be large in this region (local microturbulence in the magnetosheath) and not appropriate for the present purpose. The two times (t_e, t_f) are again only used for initializing the next automated step.

245   From the initial time estimates (t_c, t_d) and (t_e, t_f), the determination of the final times for the entry in and exit from the ramp (t_3, t_4) and (t_5, t_6) respectively, is made with an automatic algorithm. In order to characterize a steep gradient, we perform a linear fit of the data points between t_c and t_f. The time range for the regression can vary on both sides. The process is initialized by the largest possible time interval with $t_3=t_c$ and $t_6=t_f$. Then, the entry time can vary between t_c and t_d, while the exit time can vary between t_e and t_f. The choice of a linear fit mainly excludes any "pollution" of the ramp region by a part of the

250   extended foot (around the upstream edge of ramp) and by downstream fluctuations around the overshoot (around the downstream edge of the ramp). The resulting time interval is associated to the best linear regression coefficient and the bounding times (t_c and t_f) explored during the automatic procedure are kept to estimate the error bars. In other words, we impose $t_3 = t_c$ and $t_6 = t_f$. The automatic procedure only defines t_4 and t_5 (internal limits of the ramp). Then, the crossing of the downstream asymptotic value closer to the first estimate defines the exit from the overshoot (nearly equivalent to the middle

255   of the gradient between the first overshoot and the first undershoot, not shown in detail here). The times t_7 and t_8 for the exit from the first overshoot are defined in the same way as the entry (Figure 2a). The time t_g shown by a vertical blue dashed line is - as for the other microstructures- simply the initial rough 'visual' estimate and is just shown for reference for a later visual check. For every shock crossing by the Cluster quartet, we make the same procedure for each satellite. The satellite that is associated with the steeper ramp from this analysis is used to arbitrarily define what is called the 'reference satellite' for a shock

260   crossing event. Then, we determine the middle time $t_{ramp,i}$ of the ramp crossing time interval for each individual satellite 'i' and the 'reference time' for a shock crossing is simply this middle time t_{ref} for the arbitrarily chosen 'reference satellite'. We then determine the shock velocity and normal from the four different middle times $t_{ramp,i}$ and the four spacecraft positions in the GSE frame by using the classical 'timing-method' (*e.g.*, Schwartz, 1998 and Horbury *et al.*, 2001, 2002). This method works if the separation between the spacecraft is not too large (otherwise the hypothesis of a planar structure breaks down) and

265   provided that the four spacecraft are not coplanar (otherwise the method fails) and that the shape of the tetrahedron is not very elongated (which is not the case for the present study). This method provides a 'global' normal vector $\underline{\mathbf{n}}_0$ valid only at the length scale of the spacecraft tetrahedron (i.e. the largest inter-distance between two satellites) and at the temporal scale defined by the time interval between the first crossing and the last crossing among the four satellites. The error bars on the entry/exit times are used to determine an error bar on the normal vector. It must be mentioned that each local normal vector $\underline{\mathbf{n}}_i$ for the

270   crossing by s/c$_i$ can differ from the global $\underline{\mathbf{n}}_0$ because of the small-scale turbulence of the front (shock front ripples) but cannot be determined experimentally as reliably as $\underline{\mathbf{n}}_0$ by any classical single-spacecraft method. Moreover, as it will be discussed later, we intend here to compare the values determined experimentally with simulations results for which the normal vector $\underline{\mathbf{n}}_0$ and thus the θ_{Bn0} angle are 'globally' defined for a shock front both averaged spatially perpendicular to the normal and in time (see Sect. 4.4). This will also conversely justify the averaging along the shock front made in the simulations (that will be

275   described in Sect. 4.4). The local effect due to the variation of the local normal direction $\mathbf{n_i}$ with respect to $\underline{\mathbf{B}_0}$ (local curvature effect due to the shock rippling at a lower scale) is not analysed in the present work.

For all the shock front micro-structures, the above analysis gives an 'apparent' temporal extension along each satellite path and allows to compare them between the four satellites. In every individual spacecraft frame, we compute an individual shock velocity vector. Since the spacecraft velocities in the Earth frame are typically around a few km/s as also found for many

280   slowly moving shocks in the same frame, it is essential to also take this small spacecraft velocities into account. The major aim of the present analysis is to reconstruct a local spatial profile along the 'global' shock normal $\underline{\mathbf{n}_0}$ as shown in Figure 2b. For this purpose, the angle between each spacecraft 'i' trajectory and $\underline{\mathbf{n}_0}$ has been used. Then, it is possible to measure the local physical thicknesses along $\underline{\mathbf{n}_0}$ of the microstructures of the shock front and compare them between the different satellites. It must be mentioned that the shock velocity determined by the 4-spacecraft timing-method here is an averaged velocity within

285   the time interval separating the first and the last shock crossings. Then, it is supposed to be constant during this time interval and homogeneous over the spatial scale of the tetrahedron. One cannot preclude that the shock velocity can vary inside the considered time interval and that the shock motion is subject to some acceleration inward and outward. However, this possible effect can be assumed as weak if the temporal profiles of the shock crossing are quite similar in time series taken at low temporal resolution (such as on Figure 1a). On the contrary, when a sudden shock front acceleration/deceleration (due to a

290   solar wind fluctuation) occurs between the crossings by two satellites, there is a clear signature in the time series (see in Figure 3 derived from Figure 1 in Horbury *et al.*, (2002)). Panels 3b and 3c are typical cases of observations which are eliminated from our present analysis. We use the same shock velocity in the Earth's frame for the 4 crossings to derive the spatial widths along the global normal $\underline{\mathbf{n}_0}$ for any case like in panel 3a.

Then, we can compare the obtained thicknesses of the shock microstructures with physical length values predicted either

295   by theory or from numerical simulations results. It must be mentioned that using only time series can lead to wrong comparative classification of the observed crossings. A large angle between the spacecraft velocity vector and the shock front normal can produce a long crossing duration for a real very small physical thickness and also will produce a small shock speed. In summary, a particular caution is necessary to avoid conclusions deduced exclusively from the 'temporal' profiles, especially in the selection process which is often based in the literature solely on the steepness of the temporal 'gradient'.

300   In order to have a qualitative check of the determination of the global normal n0, the times series of the component Bn of the instantaneous magnetic field along this normal is systematically examined. First, this normal component is supposed to be conserved on both sides of the shock front. Second, for a nearly perpendicular shock, this component is expected to vanish (exactly zero for 90° shock) upstream from the shock front and inside the ramp, since the vector of the magnetic field is supposed to be strictly along the shock front. Figure 4 displays the temporal evolution of Bn for a shock front crossing on

305   03/31/2001 around 1738 UT for one of the four satellites (magenta lower curve) in comparison with the total magnitude B (black upper curve). For this shock, the ⬜Bn angle is about 86°. If one takes into account the fluctuations observed in and around the ramp, the conservation in the front is well respected and the upstream value is also very low as expected for a nearly

perpendicular case. The downstream evolution in the overshoot is also consistent with expected oscillations around the average downstream value (e.g., Kennel and Sagdeev, 1967).

310
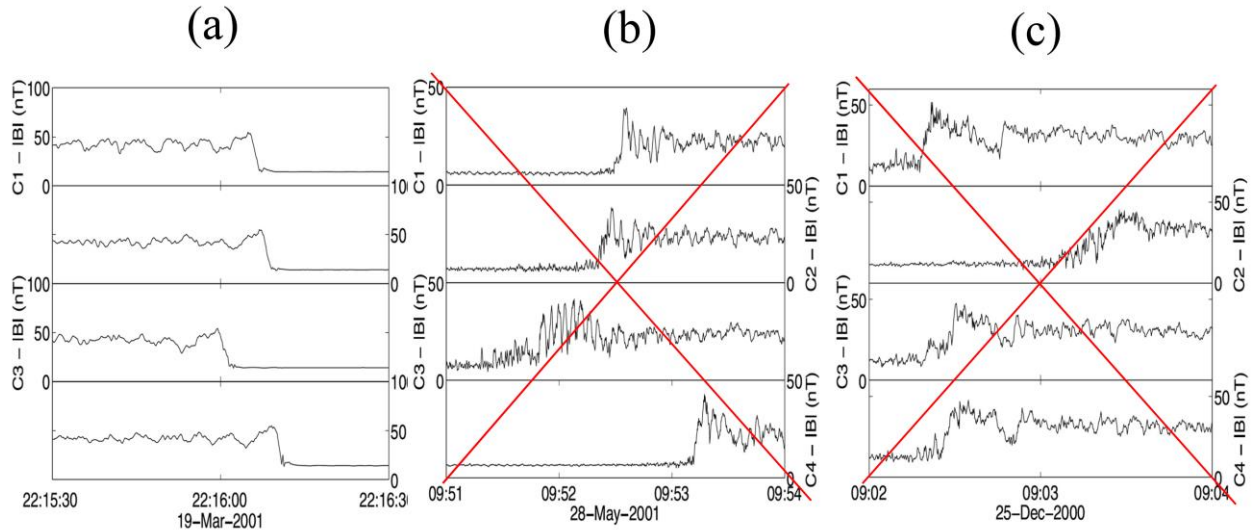
Figure 3 : Three examples of the total magnetic field amplitude measured versus time by each of the 4 Cluster satellites during 3 different shock crossings at a resolution of 5 vectors /s. Panel (a) illustrates a good (selected) example of a clean and sharp shock, while panels (b) and (c) have been rejected in our selection since the shock either exhibits a complex and disturbed profile (panel b) or the shock certainly
315 suffers an important acceleration (panel c) as evidenced respectively between the profiles measured by the 4 spacecraft (adapted from Horbury et al., 2002).

3 Analysis of individual shock crossings

3.1 One typical case

320 A typical example of the spatial profiles is shown in Figure 5. It is obtained for one supercritical quasi-perpendicular shock crossing by Cluster on 03/31/2001 at 1738 UT (θ_{Bn}=86±2°, M_A=4.1, β_i=0.05) when the s/c separation was about a few ion inertial lengths c/ω_{pi} (herein c/ω_{pi} = 80-120 km, typically). The profiles are ordered by the sequence of crossings starting from satellites C4 to C3 (top to bottom in Figures 5a and 5b). The relative locations of the four s/c defined at the 'reference time' given by satellite C4 (see Sect. 2.2) are represented in the plane containing both the X_{GSE} direction and the normal $\underline{\mathbf{n}}_0$ (Figure
325 5c) and in the plane perpendicular to the normal $\underline{\mathbf{n}}_0$ (Figure 5d).

In a first approach, the differences between the 4 s/c spatial profiles in panel 5b are quite obvious in particular for the magnetic foot and the overshoot widths; however, these are less evident for the ramp. We emphasize that all upstream conditions remain unchanged for all four satellites. As a consequence, this evidences the strong variability of the quasi-perpen-
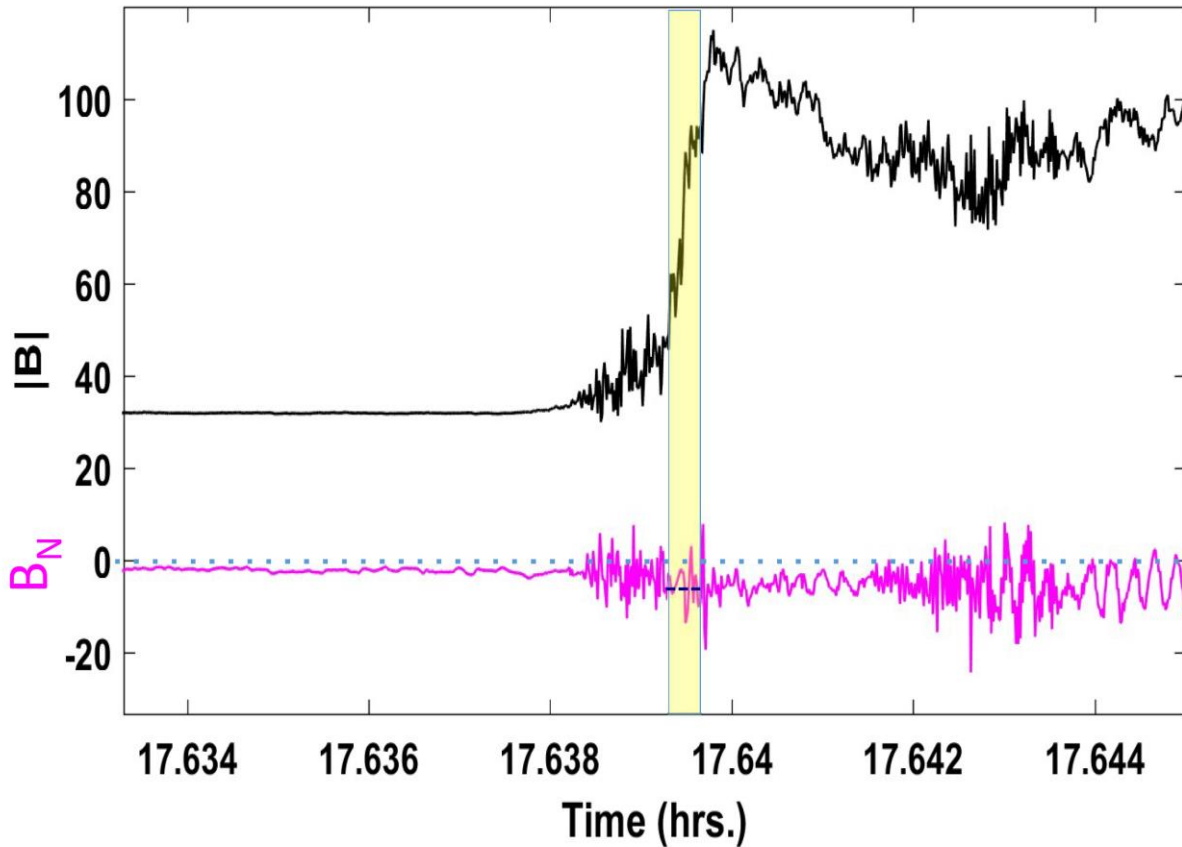
330   **Figure 4**: Time variation of the B field amplitude and of its associated B_n normal component (used to verify the criterium on the normal component; see Sect. 2) on March 31, 2001 around 1738 UT, where, $M_A = 4.1$, $\theta_{Bn} = 86° +/- 2°$, and $\beta_i = 0.04$.

dicular shock front itself. We stress that the ramp widths can be very narrow and can reach values as low as a few electron inertial lengths with the thinnest one reaching 5 c/ω_{pe} for satellite C4. This result strongly disagrees with the typical scale length of the ramp commonly considered as around c/ω_{pi} (e.g., Russell and Greenstadt, 1979; Scudder et al., 1986; Bale et al.,

335   2005) although in a very good agreement with some "exceptional" ISEE results (Newbury and Russell, 1996, 1998) as well as theoretical studies predicting the existence of small scales in quasi-perpendicular shocks as a signature of the front nonstationarity or results issued from PIC numerical simulations (Lembège and Dawson, 1987; Lembège and Savoini, 1992; Lembège et al., 1999, 2013a, 2013b; Schöler et al. 2003, Marcowith et al, 2016 and references therein).

        This nonstationarity can be also evidenced in the content of Figure 5. The satellites C3 and C4 locations are almost aligned

340   with the direction n0 (Figure 5c) and are close one to each other (over a distance less than c/☐pi) in the plane perpendicular to n0 (Figure 5d). If the shock front was stationary, after propagating from C4 to C3, the profiles would be expected nearly identical while they appear significantly different. For instance, the spatial ramp thickness for C3 is about twice the one for
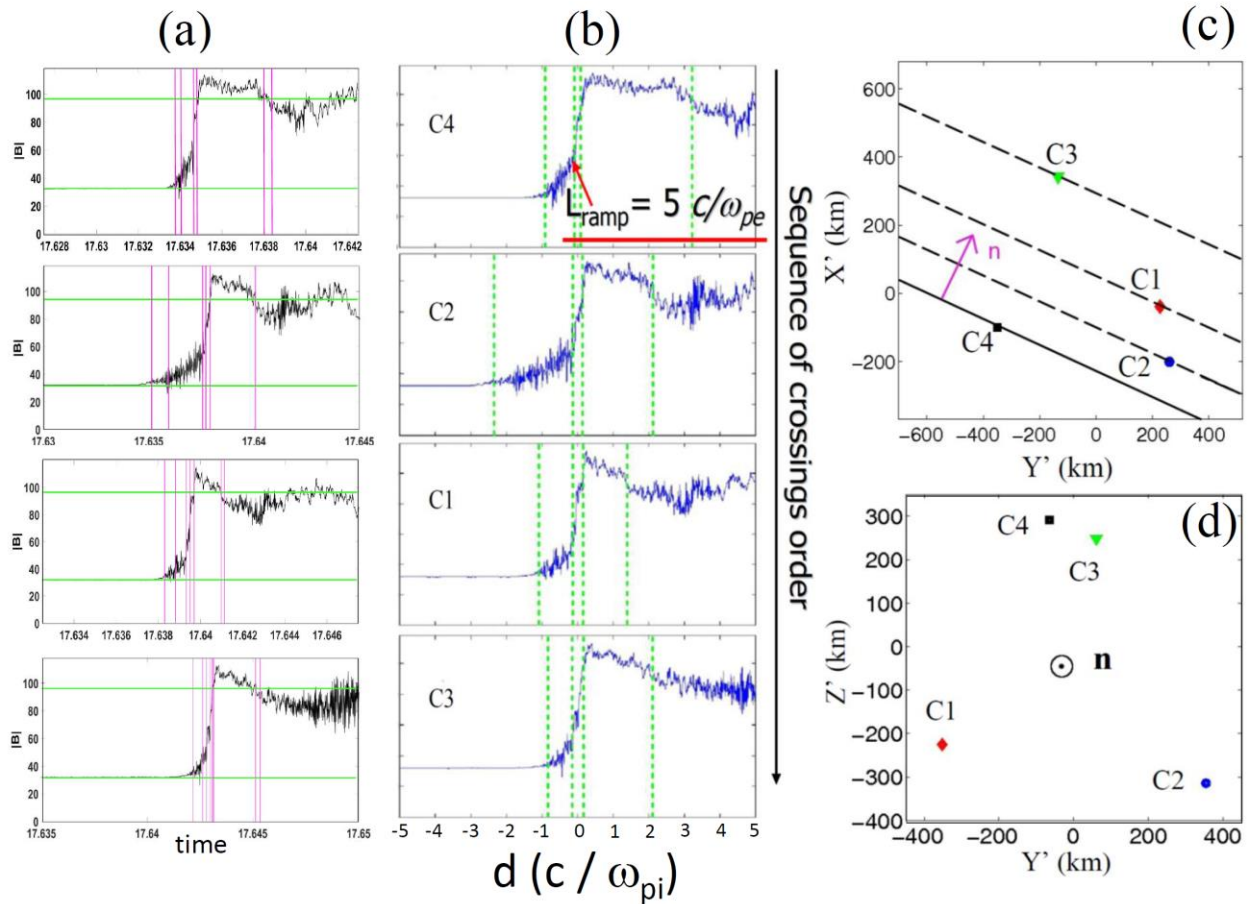
Figure 5: Time and spatial profiles along the normal of the magnetic field magnitude for the shock crossing on 03/31/2001 at 1738 UT are shown in panels (a) and (b) respectively. For this shock crossing, v_{sh} = 18 km/sec, M_A = 4.1, θ_{Bn} = 86° +/- 2°, and β_i =0.05. The locations of the 4 Cluster satellites for the event displayed at the 'reference time' t_{ref} defined for satellite C4 (see text) are reported within the plane defined by X_{GSE} and the normal $\underline{n_0}$ (panel c), and within the plane perpendicular to $\underline{n_0}$ (panel d). (Panels (b), (c) and (d) are issued from Figures 3 and 4 of Mazelle *et al*., 2010).

C4, and the shape and thickness of the overshoot are also very different. Moreover, C2 and C1 locations are not far to be along the $\underline{n_0}$ direction (Figure 5c) but they well depart one from each other in the perpendicular front (i.e. along the shock front) by several c/ω_{pi} (Figure 5d). The differences mentioned here can be related to the shock front nonuniformity due to its rippling; the impact of this rippling on the front variations will be analysed in a future work.

3.2 Impact of the shock velocity

A careful determination of the shock velocity is necessary in order to discuss the physical spatial thicknesses of the shock front substructures. This also means that it is not possible to consider only times series to discuss the relative properties of different shock crossings. Moreover, as already stated previously, the time resolution of the data needs to be considered before any

conclusion. This is illustrated in Figure 6. The left part shows the time series of the magnetic field components and magnitude for two shock front crossings and for two different time resolution each (panels a1 and b1): the highest available resolution (15 or 60 ms depending on the mode) and the spin resolution of 4s. These two shocks have been chosen as they are characterized

360   with similar parameters θ_{Bn}, M_A, and β_i. The first shock 'a' (panel a1) is a 'slow' shock with a velocity of about 11 km/s while shock 'b' (panels b1) is a 'fast' shock with a velocity of about 78 km/s. When considering the lowest time resolution (averaged data on 4s), the two profiles in the upper plots of panels 'a1' and 'b1' appear very. If only data with this time resolution were considered, one should have concluded at first glance that the two shock crossings are very similar and display very similar properties with relatively smooth time gradients of a similar shape. But, the highest time resolution on the lower panels reveals

365
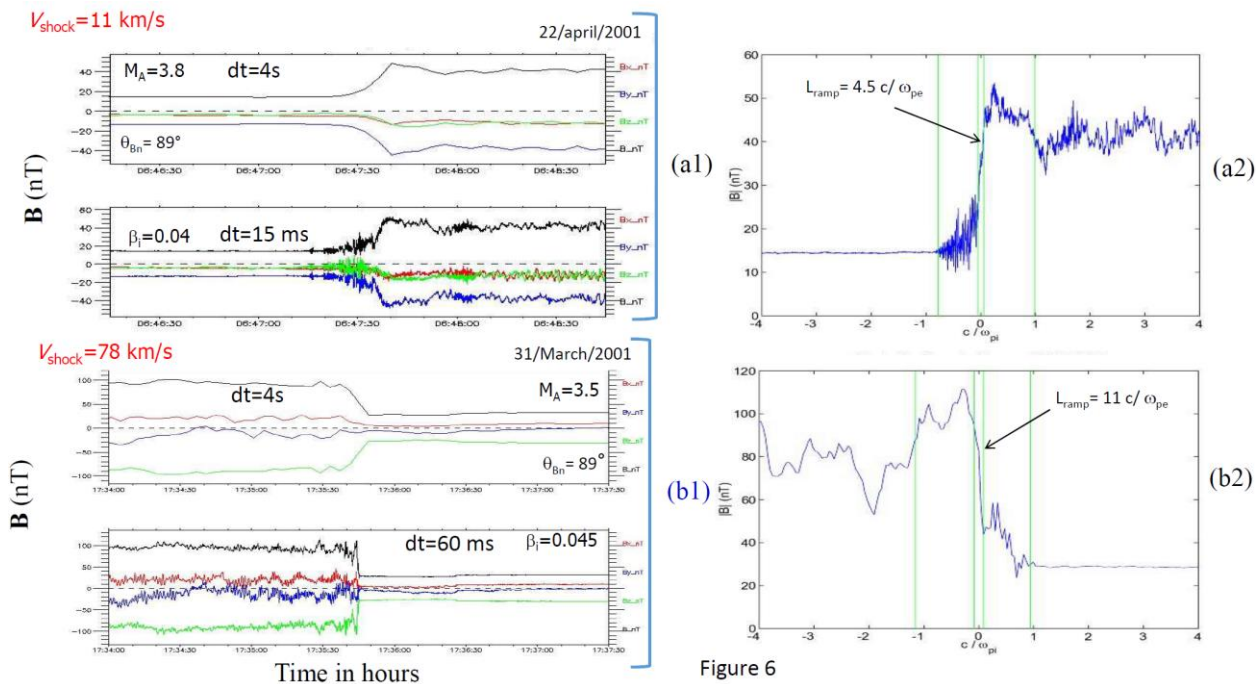
Figure 6: Comparison of a slow moving shock (panels (a1) and (a2), where v_{sh} = 11 km/s, M_A=3.8, θ_{Bn} = 89°, and β_i =0.04) and a rapid shock (panels (b1) and (b2), where v_{sh} = 78 km/sec, M_A = 3.5, θ_{Bn} = 89°, and β_i = 0.045) defined for low (dt=4 s) and high resolution rates (dt=15 or 60 ms). Panels (a1) and (b1) provide the temporal profiles of the total magnetic field amplitude (defined respectively for C1 and C3, while
370   panels (a2) and (b2) provide correspondingly the spatial profiles of the measured magnetic field (the distance is normalized with respect to the ion inertial length defined upstream). The spatial origin corresponds to the location at the middle time of the ramp crossing interval for each satellite.

the large difference between shock profiles when changing the data sampling: shock 'b' appears steeper than shock 'a'.
375   Moreover, for shock 'a', the gradient remains nearly unchanged with only superimposed higher frequency fluctuations which are not observed upstream from the sharp front displayed by shock 'b'. The full shock properties are revealed only if the spatial profiles, as shown on panels 'a2' and 'b2', are considered. The general shapes of the shock front substructures are very similar

for the two shocks, but the steeper spatial ramp is obtained for shock 'a' while shock 'b' displays a ramp spatial thickness more than twice that of shock 'a' (right hand panels (a2) and (b2) respectively). Moreover, it also reveals that the structure of the

380   shock is better sampled up to much higher frequencies for a slow shock velocity. In the spacecraft frame, any instrument like the magnetometer uses a constant sampling frequency and thus obviously gets much less measurement points inside any shock front substructure when this one is propagating faster. This example illustrates quite well the advantages of the methodology developed in the present study to correctly address the spatial scales of a shock front and the deep caution to keep in mind when analysing only the temporal shocks profiles.

385   **4 Statistical analysis**

4.1 Selection criteria

An analysis similar to the one described in Sect. 3 has been performed for a list of shocks after a severe selection procedure. Several criteria have been used: (i) limitation to shocks normal direction θ_{Bn} approaching 90° as much as possible (more than 75°) in order to avoid more complex mechanisms which take place at oblique shocks (Lembège and Savoini, 1992; Lembège

390   et al, 2004; Marcowith et al. 2016), (ii) existence of well-defined upstream and downstream ranges for each of the 4 s/c, (iii) stability of the upstream averaged magnetic field from one s/c to another, (iv) validity of the normal determination by checking the weak variability of the normal field component B_n around the ramp and low value of $B_n/|\mathbf{B}|$ upstream for θ_{Bn} close to 90°, (v) availability of all data necessary to compute the shock parameters and (vi) a maximum spacecraft separation distance limited to a few c/ω_{pi} between the four spacecraft in order to consider the crossing of a same "individual" shock front by all

395   Cluster spacecraft. From an initial ensemble of 455 shock crossings (including essentially data for 2001 and 2002 for which spacecraft separation distances are all small enough), only 24 shock events have been selected after the validation of the aforementioned criteria. This implies a detailed analysis of 96 individual shock crossings. Figure 7 displays the distributions of four main parameters θ_{Bn}, M_A, β_i and v_{sh}/v_{thi} (see Sect. 1). For the selected shock crossings, the θ_{Bn} values extend from almost 90° to 75° but mostly above 84° (80%), the M_A values of the resulting shocks are equally distributed from 2 to 6.5, the

400   ratio v_{sh}/v_{thi} between 2 and 30 with a peak within the range 12-24, and β_i extends from very low values to 0.6 but with 67% values less than 0.1.
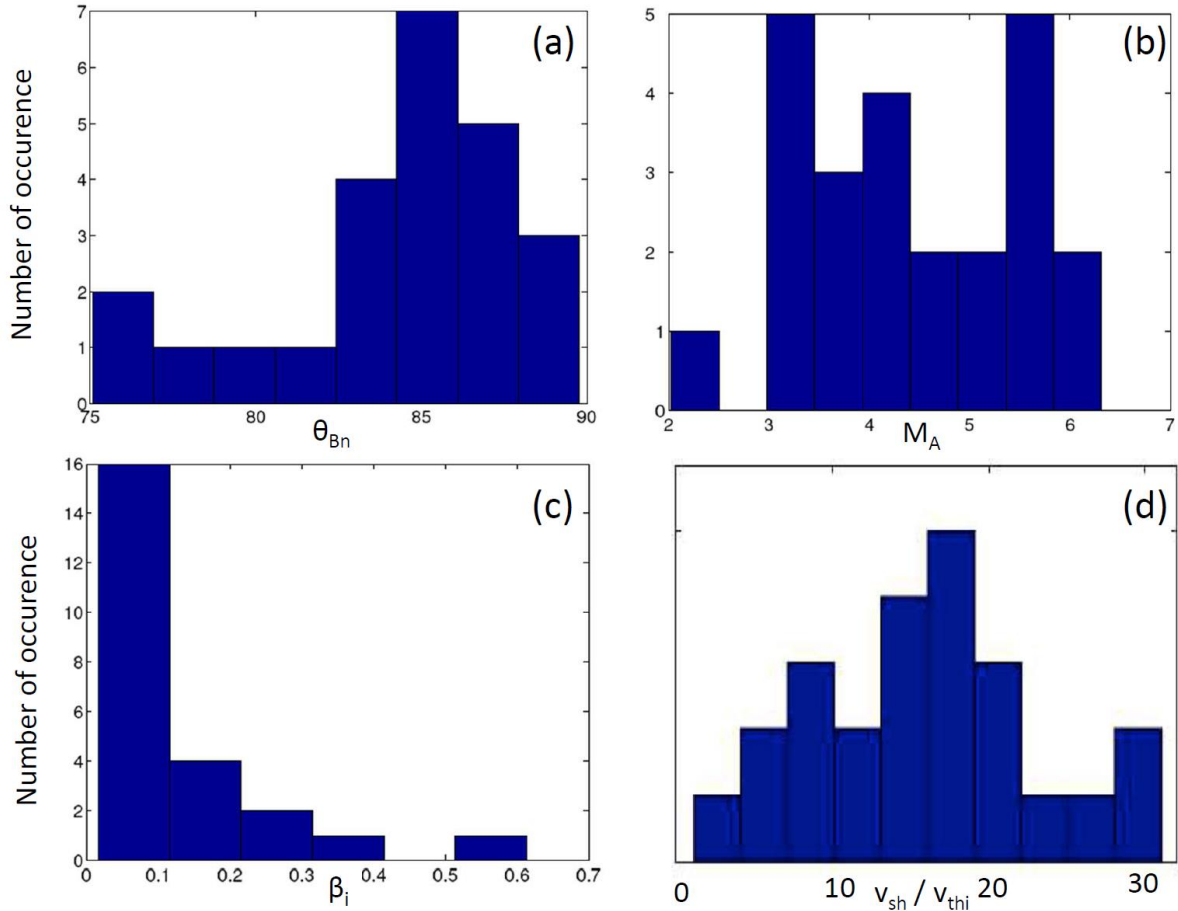
Figure 7: Distribution of the 96 (selected) shock crossings versus (a) the angle θ_{Bn} (defined between the shock normal direction and the upstream magnetic field), (b) the Alfven Mach number ($M_A = V_{sw,n} / v_A$, where $V_{sw,n}$ is the solar wind bulk velocity component defined along the shock normal, and v_A is the upstream Alfven velocity respectively), (c) the ratio β_i (between the ion thermal pressure and the magnetic pressure), and (d) the ratio v_{sh} / v_{thi} where the v_{sh} is the velocity of the shock front defined in the rest plasma frame (to be compared with present simulation results) and v_{thi} is the upstream solar wind proton velocity.

4.2 Ramp thickness

The obtained ramp thickness distribution shown on Figure 8a appears Gaussian, indicating that most of the shocks are associated with a narrow ramp. Interestingly, the distribution reveals a cut-off mark at c/ω_{pi}. Figure 8b displays the thinnest ramp found among each quartet of crossings for each individual shock versus θ_{Bn}. No simple relation emerges. However, many observed thinnest ramps have a width less than 5 c/ω_{pe} and the magnetic ramps thickness tends to reach low values when

approaching 90°. Figures 8c and 8d display scatter plots of all ramp thicknesses versus θ_{Bn} and M_A respectively; for clarity,

415   individual error bars are not reported on the figure.
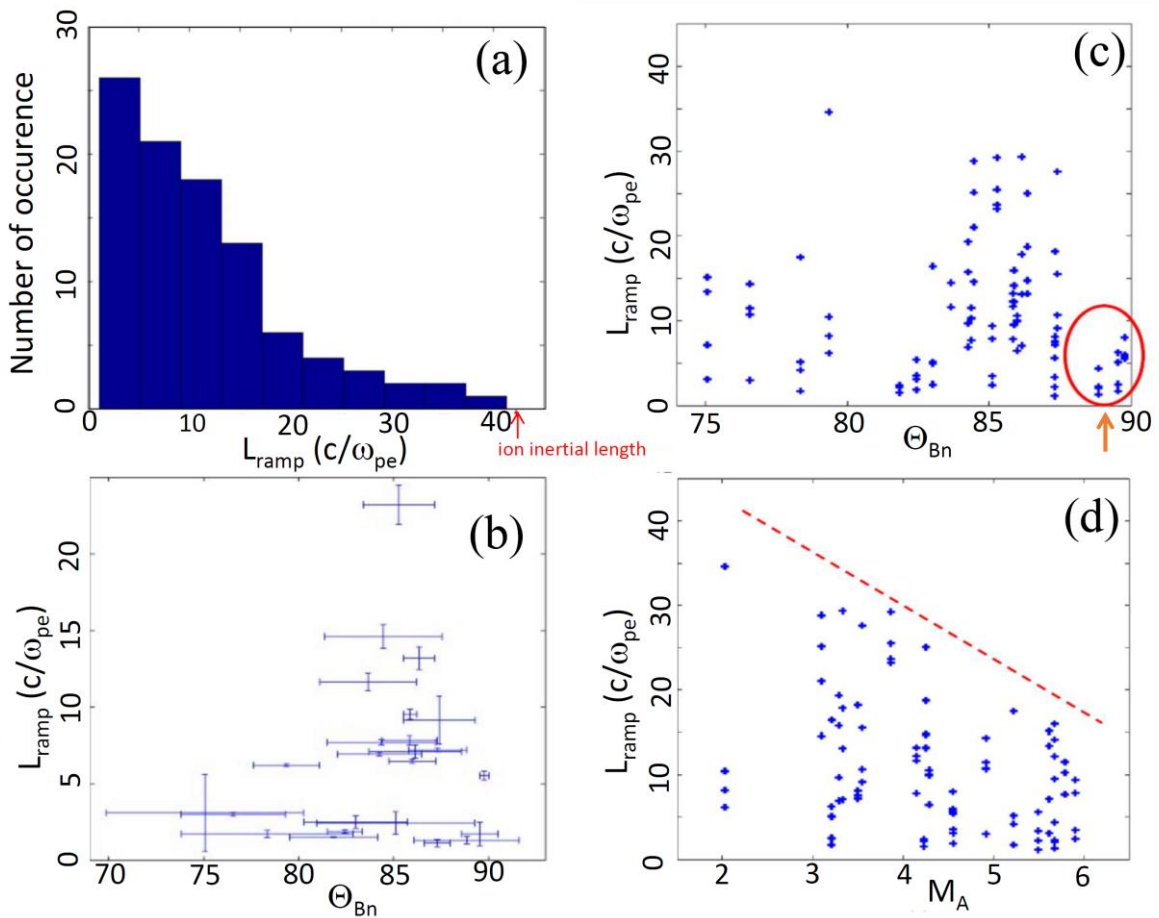
Figure 8: (a) Distribution of all ramp thicknesses measured by the 4 Cluster satellites during the 24 shock crossings (total covers 96 individual crossings). (b) Distribution of the thinnest ramp thickness observed versus the angle θ_{Bn} (defined between the shock normal direction and the upstream magnetic field); each thinnest thickness is selected among the 4 measurements made by the 4 satellites during the crossing of
420   the same shock). Panels (a) and (b) are derived from Figure 5 and 6 of Mazelle et al. (2010). Distribution of all ramp thicknesses (all spacecraft measurements mixed) versus (c) the angle θ_{Bn} and (d) the Alfven Mach number ($M_A= V_{sw,n}/v_A$) respectively; $V_{sw,n}$ and v_A are respectively the bulk solar wind velocity along the shock normal and the upstream Alfven velocity. The ellipse in panel (c) focuses on results around $\theta_{Bn}=90°$; the dashed line in panel (d) indicates the upper limit of the L_{ramp} / (c/ω_{pe}) values.

425   Although Figure 8c shows no clear dependence of the ramp width with θ_{Bn}, it however indicates that the narrowest ramps

are associated with nearly perpendicular geometries as pointed out by the red arrow. Figure 8c also shows that the ramp

thickness variation is not solely controlled by the shock-geometry. It can vary a lot for a single value of θ_{Bn} except maybe

when close to 90. No less important, the ramp thickness obtained from the analysis of a same crossing with each single s/c appear inconsistent (up to a factor 7) although the upstream conditions remain similar. This illustrates quite well the signature

430   of an intrinsic shock front nonstationarity. Figure 8d does not reveal any simple relation of the shock ramp thickness with M_A. It may only illustrate that the maximum observed thickness reduces as the Mach number increases, although the scatter plot and the statistics do not allow to make any conclusive result.

The statistics confirms the important result evidenced in the individual case study of Sect. 3, that the magnetic field ramp of a supercritical quasi-perpendicular shock often reaches a few c/ω_{pe}. The time variability of scales observed for the same

435   upstream conditions is also consistent with a signature of the front nonstationarity due to the self-reformation fed by the accumulation of reflected ions in agreement with PIC and hybrid simulations results (Lembège and Dawson, 1987; Biskamp et Welter, 1972; Lembège et al., 2004; Lembège and Savoini, 1992; Hellinger et al., 2002). Other mechanisms raising from the modified two stream instability (triggered by the relative drift between incoming electrons and reflected ions within the foot region of the front) for oblique shocks (Schöler et al., 2003) may also be responsible for the nonstationarity of the shock

440   front as discussed in Sect. 5.

4.3 Magnetic foot

The left panel of Figure 9 displays the distribution of the magnetic foot thickness for ~~all~~ the 96 shock crossings by any individual spacecraft versus the foot thickness (normalized with the upstream ion gyroradius ρ_{ci}) whereas the right panel shows the maximal value among the four satellites for each selected shock crossed by the quartet (labelled with the numbers on the

445   horizontal axis) versus the foot thickness normalized with ρ_{ci}.

First, the distribution (Figure 9a) clearly shows that the foot thickness is always found less than the upstream gyroradius. Second, most of the foot thicknesses (81%) are found to be less than 0.4 $\rho_{ci,us}$ and the median value is 0.2 $\rho_{ci,us}$. Most of the observed shocks are characterized by a foot with a thickness ($L_{foot} < 0.1$ $\rho_{ci,us}$) indicating that the foot width rarely reaches its maximal value. The literature provides different theoretical determinations of the foot thickness. Gosling and Robson (1985)

450   used the results of Schwartz et al. (1983) to show that for arbitrary angle θ_{Bn}, the upstream extent of the foot is:

$$d = \rho_{ci}\,cos\theta_{vn}\left[\,\Omega_p t'\,(2cos^2\theta_{Bn} - 1) + 2sin^2\theta_{Bn}sin\Omega_p t'\,\right] \tag{1}$$

where $$cos\Omega_p t' = \frac{1 - 2cos^2\theta_{Bn}}{2sin^2\theta_{Bn}} \tag{2}$$

455   and θ_{vn} is the angle between the shock normal and the upstream solar wind velocity vector.

Another ~~previous~~ determination was given by Livesey et al. (1984) as:

$$d = 0.68\,\rho_{ci,us}\cos\theta_{vn}\,sin^2\theta_{Bn} \tag{3}$$

For a strictly perpendicular shock ($\theta_{Bn} = 90°$) and a normal incident upstream solar wind ($\theta_{vn} = 0°$), the foot width then reaches the distance for a reflected ion at the time of its turn-around defined by $dx_n/dt = 0$, where x_n is the coordinate of the

460   ion along the normal, given by Woods (1969; 1971):

$$d = 0.68 \, \rho_{ci,us} \tag{4}$$

The values of d obtained from Eq. (1) – Eq. (2) are shown by red points on Figure 9b for each shock event. For each event, the blue value with error bar is the largest experimental foot thickness for one among the four satellites. The horizontal blue dashed line shows the theoretical value given by Eq. (4) and clearly stresses that the maximal experimental foot thickness

465   is usually below the 90°-critical value and the value obtained from the experimental derivation of θ_{Bn} and θ_{vn} (considering the error bars). Thus, for each specific shock crossing and associated parameters, the above two theoretical values which are supposed to be fixed by the two aforementioned angles (and thus not varying with time) can be generally considered as an upper bound of the observed "instantaneous" foot thickness.
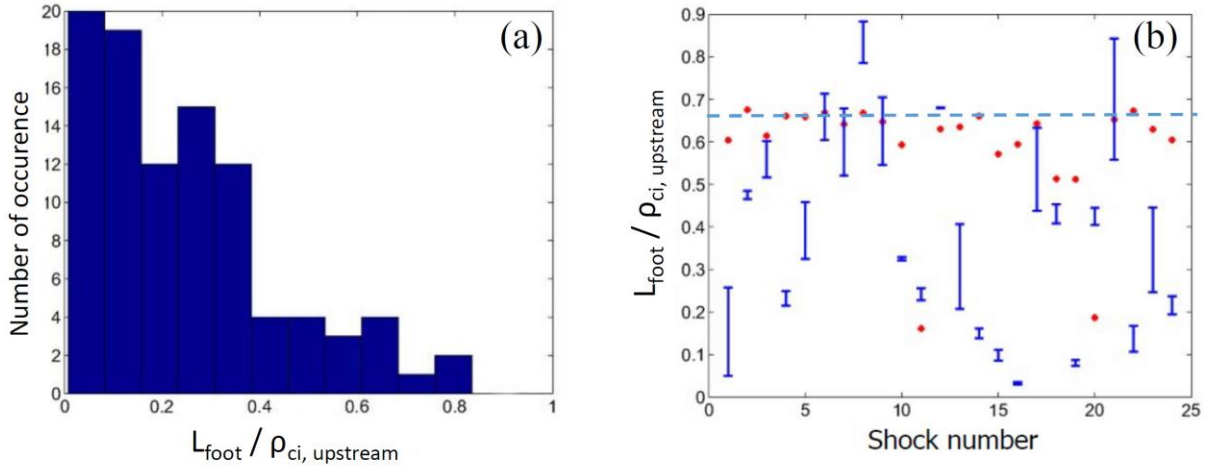
470

Figure 9: (a) Distribution of the 96 shock crossings versus the foot thickness (normalized versus the upstream ion gyroradius $\rho_{ci,us}$); (b) Distribution of the largest experimental foot thickness (normalized versus the upstream ion gyroradius $\rho_{ci,us}$) for every shock event; the vertical bars correspond to the error estimate made on the measured values in blue, and the red dots correspond to the upper bound values i.e. the theoretical values obtained from Eq. (1-3) of Sect. 4.3 (i.e.. Eq. 3 of Gosling and Robson, 1985). For reference, the value $L_{foot} / \rho_{ci,us}$
475   = 0.68 defined for θ_{Bn} = 90° (Woods, 1971) is indicated by the blue horizontal dashed line in panel (b).

4.4 Comparison with numerical simulation results.

To compare more precisely with numerical simulation results, two-dimensional PIC simulations (where both ions and electrons are treated as individual macroparticles) have been performed like those of previous works (Lembège and Savoini, 1992;
480   Lembège et al., 2009), where the planar shock is initialized by a magnetic piston (applied current pulse). Therefore, the shock geometry is always defined in the upstream frame: the shock propagates along the x direction. Periodic conditions are used along the direction of the planar shock front (y-axis). Herein, the shock is strictly perpendicular (θ_{Bn} = 90°) where the upstream magnetostatic field B_0 is along z axis, and propagates within the (x-y) simulation plane; this perpendicular shock is used as a reference case. All quantities are dimensionless, are indicated by a tilde ' ~" and are normalized as follows : the spatial

485   coordinate is $\tilde{x} = x/\Delta$; velocity $\tilde{v} = v/\omega_{pe\Delta}$; time $\tilde{t} = \omega_{pe}t$, electric field $\tilde{E} = eE/m_e\omega_{pe}^2{}_\Delta$; magnetic field $\tilde{B} = eB/m_ew_{pe}^2{}_\Delta$. The

parameters e, m_e , $_\Delta$, and ω_{pe} are respectively the electric charge, the electron mass, the numerical grid size and the electron

plasma frequency. These definitions are identical to those used in previous 1-D PIC (Lembège and Dawson, 1987), and 2-D

PIC simulations (Lembège and Savoini, 1992). The plasma conditions and shock regime used herein are similar to those used

in Lembège et al. (2009). All basic parameters are summarized as follows: the plasma simulation box has 6144 x 256 grids

490   with a spatial resolution $\Delta=\Delta x=\Delta y=\Delta z=1/60$ ($\tilde{c}/\tilde{\omega}_{pi}$) = 1/3 ($\tilde{c}/\tilde{\omega}_{pe}$) (where $\tilde{c}/\tilde{\omega}_{pi}$ and $\tilde{c}/\tilde{\omega}_{pe}$ are the upstream ion and

electron inertial lengths respectively), which is high enough to involve all microstructures of the shock front. Initially, the

number of particles per cell is 4 for each species. Velocity of light $\tilde{c}$ = 3, and mass ratio of proton and electron M_i/m_e =

400. To achieve reasonable run times and simulation domains, a ratio of $\tilde{\omega}_{pe}/\tilde{\omega}_{ce}$ = 2 had been used as in Hada et al. (2003)

and Schöler and Matsukiyo (2004). The electron/ion temperature ratio is $T_e/T_i = 1.58$; upstream ions and electrons are isotropic

495   so that $\tilde{v}_{thi=} = \tilde{v}_{thi,x,y,z}$ and $\tilde{v}_{the} = \tilde{v}_{the,x,y,z}$ respectively. The ambient magnetic field is $\tilde{B}_0= 1.5$. The shock has an averaged

Alfvenic Mach number, $M_A = \tilde{v}_{shock}/\tilde{v}_A = 5.06$ where the upstream Alfven velocity $\tilde{v}_A$ is equal to 0.075 and the shock velocity

$\tilde{v}_{shock}= 0.38$. The ratio $\tilde{\beta}$ of upstream plasma thermal pressure to magnetic field pressure is taken as $\tilde{\beta}_i = 0.10$ for protons and

$\tilde{\beta}_e = 0.16$ for electrons. For these initial conditions, all other upstream plasma parameters are detailed in for both electrons and

protons.

500   In present plasma conditions, cycles of the shock front self-reformation are evidenced like those of previous works

(Lembège and Dawson, 1987; Lembège and Savoini, 1992, Lembège et al., 2009). An enlarged view of the time stackplot of

the (y-averaged) main magnetic field component is shown over one cycle in Figure 10a. Note that the local direction of the

front normal versus the upstream magnetostatic field is varying along a front ripple. Then, considering an average along the

shock front (y-axis) is equivalent to averaging over these local normal directions and agrees with the method used in

505   experimental data for determining the normal direction of the shock front crossed by the Cluster tetrahedral configuration for

small satellite inter-distance (i.e. average over local normal directions given individually by each satellite).

As shown in previous works, the self-reformation is mainly characterized by (i) a strong cyclic magnetic field amplitude

variation at the overshoot with a time period $\tilde{\tau}_{ref}(= 1523)$ of the order of 1/3 $\tilde{\tau}_{ci}$ (where $\tilde{\tau}_{ci} = 5027$ is the upstream ion cyclotron

period) so that several self-reformations can take place within one upstream ion cyclotron period; (ii) a temporal anticorrelation

510   of the B field amplitude measured at the foot and at the overshoot respectively, and (iii) a strong time variability of the shock

front width. These features persist quite well even when using a realistic mass ratio as shown by Lembège and al. (2013a,

2013b); in particular, the self-reformation cyclic period does not depend almost on the mass ratio. Moreover, the features of

the other self-reformation process due to the MTSI (for slightly oblique shocks, see Sect. 1) also persists for realistic mass

ratio as shown by Schöler and al. (2003).

515

	Symbol	Electrons	Ions
Thermal velocity	$\tilde{v}_{thx,y,z}$	0.3	0.012
Debye length	$\tilde{\lambda}_D$	0.42	0.34
Larmor gyro radius	$\tilde{\rho}_C$	0.84	270
Inertia length	$\tilde{c}/\tilde{\omega}_p$	3.0	60
Gyro frequency	$\tilde{\omega}_c$	0.5	0.0012
Plasma frequency	$\tilde{\omega}_p$	1.0	0.05
Gyro period	$\tilde{\tau}_c$	13	5027
Plasma beta	$\tilde{\beta}$	0.16	0.101

Table 1. Upstream Plasma Parameters Defined for the 2-D PIC simulation

4.4.1 Results on the ramp thickness

Herein, the spatial ramp width is identified within the shock front by a linear fit defined in the steepest part of the magnetic field gradient (Figure 10b). However, the procedure to define this width slightly differs from that used for Cluster experimental data in Sect. 2. Presently, its lower bound (dashed line B) is defined where the B profile departs clearly (due to the foot region) from this linear fit. On the other hand, its upper bound (dashed line C) is defined where the B profile departs clearly (due to the proximity of the overshoot) from this linear fit. We do not use the overshoot as the upper bound since it is polluted by reflected ions as these gyrate and penetrate downstream after being once reflected at the ramp (Leroy et al., 1982); then this would overestimate the ramp width. On the other hand, let us note that using the mean downstream B field as a reference (as done for experimental data analysis in Sect. 3) may be a source of inaccuracy when applied to the present numerical simulation results. Indeed, the size of the downstream region is not long enough to deduce a precise estimate of the averaged downstream B value. In the B profile of figure 10b, these lower and upper bounds are respectively
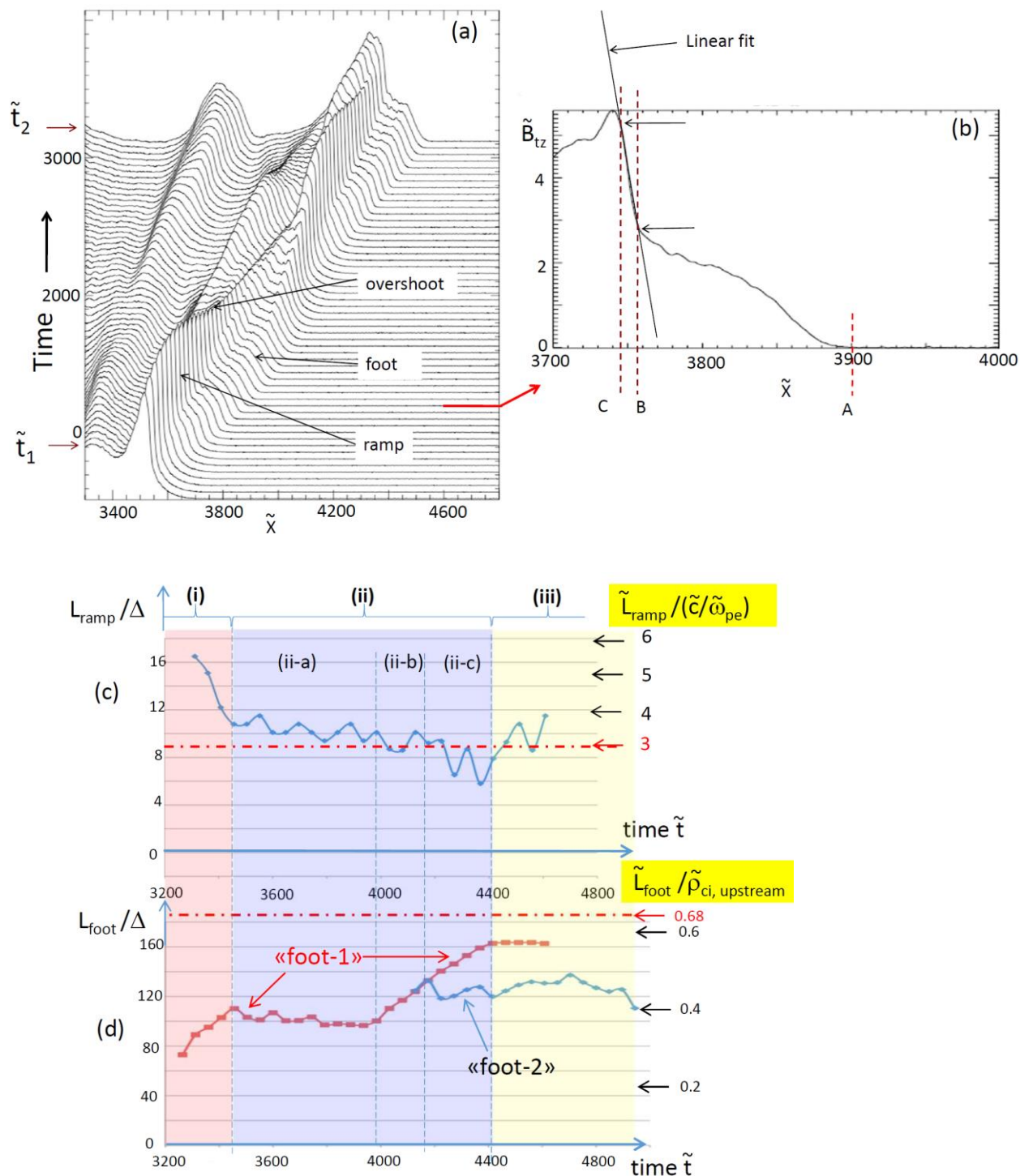
Figure 10: (a) Time stackplot of the main magnetic field component $\tilde{B}_{tz}$ versus axis $\tilde{x}$ (the time evolves from the bottom to the top curve, and the propagation of the shock front is along $\tilde{x}$ axis from the left to the right-hand side). Results are issued from 2D PIC simulation (where

545   the $\mathbf{B_o}$ static field is out of the simulation plane $\tilde{x}$-$\tilde{y}$); the $\tilde{B}_{tz}$ profile has been space-averaged along $\tilde{y}$ axis; the temporal interval between
two successive curves is $\Delta \tilde{t}$ = 48 and the time stackplot covers the time interval ($3456 < \tilde{t} < 6048$); (b) blow-up view of the spatial profile
of the main magnetic field component $\tilde{B}_{tz}$ defined at a fixed time ($\tilde{t}$ = 4128) indicated by the red arrow in panel (a); the locations of
the bounds A, B and C are illustrated by vertical dashed lines. Time history (c) of the ramp thickness measured within the range BC (defined
in panel b) normalized versus the upstream electron inertial length c/ω_{pe} (right hand side scale), and (d) the foot thickness measured within

550   the range AB (defined in panel b) normalized versus the upstream ion gyroradius ρ_{ci} (right hand side scale), during a cyclic self-reformation
period ($\tilde{\tau}_{ref}$=1523). In panels (c) and (d), the spatial widths are normalized versus the unit space grid Δ on the left-hand side scale. The
respective lower and upper bound values of the ramp and the foot thickness are reported by red dashed-dotted horizontal lines in panels (c)
and (d) respectively. Note that the width of "ramp-1" only is represented in panel (c) in order to avoid overwhelming the plot; the smalltime
fluctuations in ramp-1 correspond to error bars of the measurements (which are based on y-averaged $\tilde{B}_{tz}$ profiles).

555   located at $\tilde{x}$ = 3755 and 3745 which provides a ramp thickness $\tilde{L}_{ramp}$=10. Repeating the same measurement procedure at

different times within the self-reformation cycle allows to evidence that the ramp thickness stays always very narrow around

a (time averaged) value of $\tilde{L}_{ramp}$= 3 /$\tilde{\omega}_{pe}$ (Figure 10c); the width of the ramp is almost independent of time and of the strong

fluctuations of the maximum B field amplitude at the overshoot (not shown herein), which is mainly driven by reflected ions

(Leroy et al., 1982). Since one has to compare statistical results of experimental observations with simulations, it is important

560   to clarify the following points : (i) considering a perpendicular shock represents a reference case in the sense the ramp is

expected to be the thinnest for 90°, as compared with oblique cases (lower than 90°), indeed, whistler wave emission (precursor)

in oblique shocks tends to extend the thickness; (ii) herein, the concerned simulation is based on a relatively low $\tilde{\beta}_i$ value

(= 0.10) or equivalently a high ratio $\tilde{v}_{shock}/\tilde{v}_{thi}$ (= 31.66), which fits with the range of experimental conditions where data sets

of shock crossing have been chosen (Figure 7d); (iii) over a full self-reformation cyclic time period, the shock front covers a

565   distance of $\Delta \tilde{x}$ = 597 (or equivalently 9.8 $\tilde{c}/\tilde{\omega}_{pi}$). In the case study shown on Figure 5c, the satellites inter-distances along

the normal are respectively 1.4 c/ω_{pi} for C4-C2, 1.6 c/ω_{pi} for C2-C1, and 2.6 c/ω_{pi} for C1-C3 which makes the total distance

for the shock crossing of 5.6 c/ω_{pi}; (iv) shock curvature effects and front rippling of the shock front have been neglected herein,

in order to approach the experimental conditions where the inter-distance between satellites is small. The y-averaging of the

simulated planar shock is in agreement with the hypothesis of considering locally a planar shock front in experimental data for

570   estimating the relative speed of each satellite versus the shock velocity. Then one can extract at present the width of the fine

structures (foot and ramp) of the shock front mainly along the shock normal with a good accuracy. Moreover, in contrast with

the methodology used for experimental data (Sect. 2), it is not necessary to use herein two different levels of identification

('visual' and 'automatic') for defining the upper and lower bounds of each microstructure (ramp and foot), since profiles have

been already enough smoothed out by the y-averaging.

575   Let us remind that this self-reformation process reveals to be a very robust mechanism since it has been evidenced in PIC

and hybrid simulations (Hellinger et al., 2002, 2007; Lembège and al., 2009; Yuan et al., 2009). It was observed originally in

1D PIC (Biskamp et Welter, 1972; Lembège et Dawson, 1987), later in 2D PIC (Lembège et Savoini, 1992) and in 3D PIC

simulations (Shinohara et al., 2007). As will be discussed in Sect. 5.1, this self-reformation process persists well even in the

presence of microinstabilities developing within the front for perpendicular shocks (Muschietti and Lembège, 2006). The

580 variation of the ramp width versus time reported in Figure 10c shows that three successive time ranges can be defined where respectively the width decreases (range (i) defined by $\tilde{t} < 3456$), very slightly decreases (range (ii) defined by $3456 < \tilde{t} < 4400$), and increases (range (iii) defined by $\tilde{t} > 4400$) as represented by pink, blue and yellow areas respectively. Then, the width stays almost constant during a large time range (ii). Within this range, the width reaches a lower bound value around 3 c/ω_{pe}, (dashed-dotted red line) which can be used as a reference scale in the comparison with experimental data instead of

585 comparing exact scales measured at a given crossing time of the shock. In order to analyze the whole-time variation of the ramp width in detail, it can be associated with that of the foot and with ion phase space as described in Sect. 4.4.2.

4.4.2 Results on the foot thickness

On the same, Figure 10d shows the time variation of the foot width issued from the same PIC simulation. The upstream edge of the foot (vertical dashed line A in Figure 10b) is defined as the location where the magnetic field has increased by 6.67%

590 over its upstream value (Burgess et al., 1989; Yang et al., 2009, 2011). The value 6.67 % has been determined as corresponding to the maximum amplitude in the magnetic field fluctuations measured upstream (which is sensitive to the particles number per cell). Then, the amplitude of the upstream magnetic field turbulence is below the value (1 + 6.67%) x B_o in our simulations.

The time variation of the foot width can be detailed with the help of the three time intervals defined for the ramp thickness in Sect. 4.4.1, and is associated to the ramp as follows. In range (i), the foot width increases in anticorrelation with the ramp

595 variation; at that time, reflected ions are accelerated at the ramp and only initialize their gyromotion (not shown herein). The range (ii) (where the ramp width slightly decreases) includes three successive phases for the foot dynamics: one (ii-a) where the foot width is constant ($3456 < \tilde{t} < 3984$), another (ii-b) where the foot width strongly increases ($3984 < \tilde{t} < 4176$), and a last one (ii-c) where the foot width is still increasing, but in addition a secondary foot can be identified upstream (blue curve for $\tilde{t} > 4176$); a double foot appears as detailed below. Finally, in range (iii) ($\tilde{t} > 4416$), the foot width reaches a maximum

600 value ($L_{foot} / \rho_{ci,us}$) = 0.6 which remains constant at later times while the ramp thickness starts increasing.

A detailed analysis of the ion phase space (not shown here) at these corresponding time intervals allows to interpret more precisely the time variation of both ramp and foot thicknesses. In range (i) (i.e. $\tilde{t} < 3456$), the ramp (named ramp-1) is freshly formed from the steepening of the foot resulting from the previous self-reformation and the foot in panel (d) is only due to the old reflected ions (previous self-reformation) still located upstream of the new ramp-1 while accomplishing their

605 full gyration (before being transmitted downstream); this steepening corresponds to the decrease of the ramp width (range (i) in panel (c)). In range (ii-a), the ramp-1 starts to accelerate and reflect new upstream ions, which add to old reflected ions which did not reach the downstream region yet. Then, the local foot (named foot-1) is composed with two (old and new) reflected ion populations (reflected at two successive reformation cycles). During this acceleration phase, the energy of macroscopic fields at the ramp is transferred to newly reflected ions, which smooths the local steepening and the ramp-1 width

610 slightly decreases only. Within the range (ii-b), all old reflected ions have reached the downstream region; only freshly reflected ions are present upstream of the ramp, continue their gyromotion and contribute to the foot-1. Consequently, the foot-1 width

strongly increases as mainly carried by these newly reflected ions. Correspondingly, the width of the ramp-1 still slightly decreases. But, more and more new ions are reflected and accumulate in time, and a local new foot (named foot-2) builds up. This ion accumulation is large enough so that the upstream edge of this new foot-2 steepens and becomes a new ramp

615 (named ramp-2, not shown in panel (d)) which starts reflecting new ions; let us mention that the width of "ramp-2" cannot be precisely identified before $\tilde{t} < 4368$ by using the best linear fit (as in Figure 10b) since this part of the front microstructure is still mainly dominated by the growing foot (steepening is not strong enough in the upstream edge of "foot-2" within this time range). This new foot-2 (blue curve in panel d) co-exists with the old foot-1 (red curve) within the same time interval $\tilde{t} >$ 4176. Simultaneously, the amplitude of the new overshoot (not shown herein) associated to the new ramp-2 increases and the

620 field gradient between the old and the new overshoot becomes weaker. Therefore, the ramp-1 width increases at later time (time range (iii)). For $\tilde{t} > 4608$, the old ramp-1 is totally absorbed in the shock profile (between the old and the new overshoots), and its width cannot be identified precisely.

Then, the shock front may acquire a multi-peak profile including traces of old and new successive ramps (not to be confused with emission of large amplitude whistler waves emitted from the main ramp). The width of the whole shock front

625 is the summation of the ramp and the feet contribution and can be estimated from the upper edge of the new foot-2 to the lower edge of the old ramp in the front. Present results provide maximum value measured at the final stage of self-reformation cycle ($\tilde{L}_{\text{shock,max}}= 176.3 = 2.93 \ \tilde{c}/\tilde{\omega}_{\text{pi}}$ at $\tilde{t} = 4608$). Let us stress that this value represents an upper bound of the shock front width and not a common measurement of the front width itself.

5 Comparison with some previous works

630 This section is dedicated to comparing the present results with those issued from previous works. The main emphasis is given not only on the agreement/disagreement observed between the different results, but also –and even more importantly- on the strategy used in previous works for "extracting" the spatial width of the shock front microstructures. We will distinguish previous works dedicated to measurements of the ramp and of the foot thicknesses respectively.

5.1 Spatial measurements of the ramp thickness

635 *Newburry and Russell (1996)*

Most works based on the analysis of experimental data issued from ISEE 1 & 2 satellites indicate a scaling of the ramp width within the ion inertial length. In a very detailed analysis of a single shock crossing, Scudder et al. (1986) have reported the ramp thickness to be 0.2 c/ω_{pi} , a measurement which was based on an exponential fit of the foot-ramp transition. By using the same fit technic, Russell and Greenstadt (1979) have measured a slightly thicker ramp of about 0.4 c/ω_{pi} in an initial study of

640 ISEE bow shock observations. Later on, Newburry and Russell (1996) has analysed seven nearly perpendicular shocks (θ_{Bn} >80°) and found a range of ramp widths (based on a linear fit to the ramp transition) from 0.5-0.8 c/ω_{pi}. However, in one case

the ramp width was particularly thin 0.05 c/ω_{pi} (= 2 c/ω_{pe}). To the knowledge of the authors, it was the first time that a so thin ramp has been observed associated to the terrestrial shock. All the observations lead to the following statements:

a) In contrast with the tentative explanations proposed at that time (summarized in Newburry et al., (1998)), this very thin ramp (2 c/ω_{pe}) takes a full meaning herein and is in quite good agreement with the present statistical results. It represents quite well a potential signature of the self-reformation process which allows the ramp to access to very small thickness (a few c/ω_{pe}).

b) one question raises up: why most previous works evidence mainly a ramp width scaling with a noticeable part of the ion inertial length (except the very narrow ramp mentioned above) in contrast with the present results? Several answers can be proposed: First, the method commonly used in previous works and based on exponential fitting to the foot-ramp region is not appropriate to measure carefully the ramp and foot thickness respectively, since both fine structures were mixed together. This fitting methodology is a source of important errors. Second, the solar wind conditions corresponding to the set of shock crossings chosen at that time need to be verified carefully. Indeed, as β_i is relatively low ($\beta_i = 0.17$ as in Hada et al. (2003), or equivalently v_{sh}/v_{thi} equals several decades as in Scholer et al., (2003)), the reflected ions describe a focussed (narrow) beam during their gyration These maintain a well coherent gyromotion which forces them to accumulate at a certain distance from the ramp and to initialize the foot. The growth of the foot separates clearly from the ramp and is characterized by a trapping loop in the ion phase space; self reformation takes place and the front is nonstationary.

In contrast, as β_i is relatively high ($\beta_i = 0.35$ as in Hada et al., 2003, or v_{sh}/v_{thi} equals a few units as in Scholer et al., 2003), the reflected ions rapidly diffuse as these start their gyromotion; these lose their large coherent motion and spread out within the whole front (no clear ion trapping loop). The foot grows up but does not separate from the ramp. Then, ramp and foot are mixed, and a larger ramp thickness is expected as shown in PIC simulations of Lembège et al. (2013a, 2013b). Then, no self-reformation can take place and the shock front is stationary.

Newburry et al. (1998)

At the ISEE 1 & 2 time, the ramp was usually characterized by two different scales: (i) a large scale (or global ramp width) within which the main transition from upstream to downstream magnetic fields takes place, and (ii) a thinner subramp scale which contains steep jumps in the magnetic field with amplitudes sometimes comparable to the overall change in the magnetic field at the shock. One conclusion (Newburry *et al*., 1998), was that both scales are characteristic of the quasi-stationary shock profile (which -at that time- was considered as stationary within the ion gyroperiod). More precisely, Newburry *et al*. (1998) have analysed a set of 20 shock crossings and found that the width of the overall ramp transition is typically within the range 0.5-1.5 c/ω_{pi} which is quite large as compared with our present measurements. This difference can be easily explained by the fact that the authors have defined the ramp thickness based on a linear fit of the total magnetic field profile from the foot to the overshoot, which enlarges the estimate of the ramp thickness, as compared with the present method used in Sect. 3 and 4.

Cluster data and present statistical results allow to correct this view within the frame of the intrinsic shock front self-
675   reformation. The so called "large scale" of the ramp presents a large width variability (extending from a part of the ion inertia
length to a few electron inertia lengths as in Fig. 8a), which was not observed at that time for the reason mentioned above. But,
simultaneously, the so called "small scales" can result from instability developing with the foot region as the ECDI which
holds for "Electron Cyclotron Drift Instability" (Muschietti and Lembège, 2006) or MTSI (Schöler et al., 2003; Matsukyio
and Schöler, 2003; Muschietti and Lembège, 2017) for instance, and can propagate (convection effects). In present work, the
680   use of a linear fit applied within the ramp region only (as described in Sect. 3) allows to average these local small scale
fluctuations and to measure the ramp width with minimizing errors. Analysing small scale field fluctuations (as those also
observed within the ramp in Figure 2) requires a further investigation which will be presented elsewhere.

Bale et al. 2003

685   From the spacecraft floating potential measured on board of the four Cluster satellites, Bale et al. (2003) have determined the
electron plasma density, and studied the macroscopic density transition scale at 98 crossings of the quasiperpendicular
terrestrial bow shock. This first tentative for measuring the shock transition width from Cluster data was attractive but contains
several limitations for the following reason: an hyperbolic tangent function has been fitted to each density transition in order
to capture the main shock transition but no microstructures of the front –as foot, ramp, overshoot- have been identified and
690   scaled. Such a fit partially includes parts of the shock front outside the ramp itself so that it cannot apply to determine the ramp
thickness with acceptable accuracy since both ramp and foot structures are not separated. This technique takes into account
only the widest transition scale at the shock, which overestimates the ramp width and restricts drastically its application. Then,
the conclusions stating that for high Mach number shocks (including the range M_A=4-5 as that considered in the present work),
only the convected gyroradius is the preferred scale for the shock density transition are strongly questionable since the real
695   ramp is much thinner. This resulting scale corresponds to the scale of the foot rather than that of the ramp and no conclusive
statements can be obtained.

On the other hand, in the light of Cluster data, looking for an estimate of the shock transition presents nowadays a
limited interest, since recent results show that terrestrial shock is rather nonstationary and a "unique" typical spatial scaling
must be replaced by some interval or bounds of variation (lower bound/upper bound) within which the spatial scales of the
700   fine structures can vary.

Figure 11 helps to better compare our results with those by Bale et al. (2003) which have been reproduced on Figure
11a, 11b and 11d. The same representation as on panels 11b and 11d has been used for panels 11c and 11e to plot the front
thickness computed as the sum of the ramp and the foot thicknesses from our methodology versus the magnetosonic Mach
number M_{ms}. The pink area on panel 11b illustrates the range of M_{ms} explored from the present study. Figure 11c reveals that
705   in this range of M_{ms} values no clear dependence considering the large error bars (as on above panel 11b) can be identified from
the present study. It would be obviously impossible here to conclude that the front thickness simply increases with M_{ms} and
conversely the best fit would conclude here that there is a trend to decrease. Our results are therefore in strong contradiction

with conclusions of Bale et al. (2003). Moreover, if we consider another M_{ms} range of similar extension as the one shown on panel 11c from our study and highlighted by the green area on panel 11b, a similar representation (not shown here) would

710 conclude to exactly the opposite to what the dotted line on panel 11b shows, considering again the large error bars. This illustrates again the impossibility to make a simple scaling of the front thickness by a single parameter as the magnetosonic Mach number. Panel 11e shows that the front thickness normalized by the downstream gyroradius is more or less consistent with the results of Bale et al. (2003) shown on Panel 11d. There is a trend there to decrease with M_{ms} increase. As mentioned in the present study, the use what of the so-called 'density transition scale' by Bale et al. (2003) shown in Figure 11a is

715 inappropriate since it mixes the time variability of the ramp and the ion foot. They also mention a stationary shock from their Figure 1. But, this Figure does not show the highest temporal resolution of the magnetic field data but only corresponds to 5 values per second. For many shock crossings used in the present study, the profiles displayed at 5 Hz look very similar whereas the highest time resolution profiles clearly reveal different features (as illustrated on Figure 5).
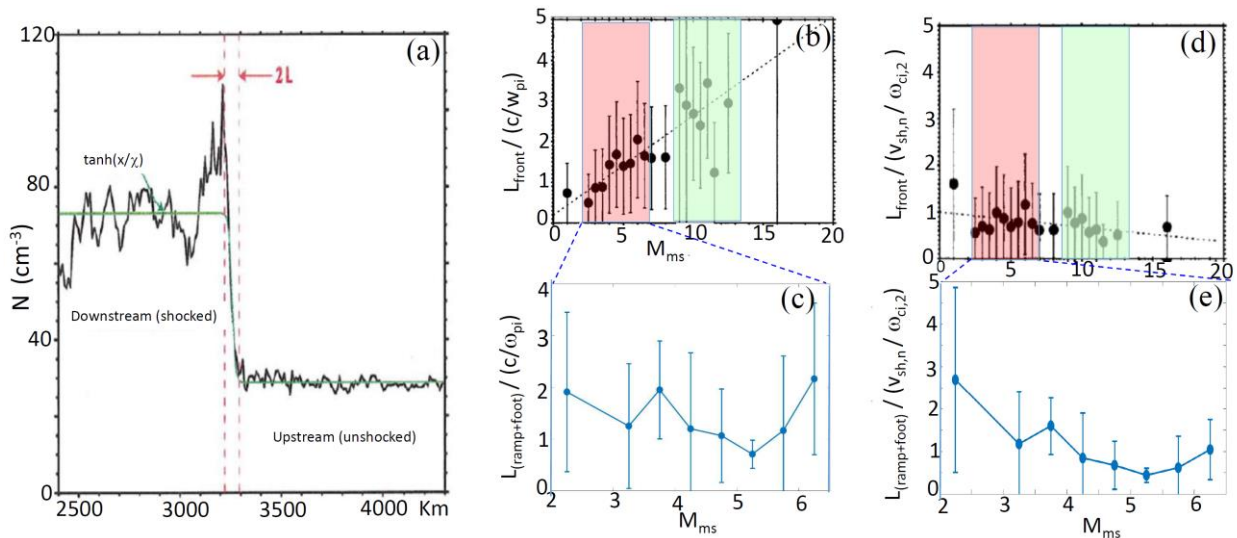
720

Figure 11: Panels (a), (b) and (d) are issued from Figures 3 and 6 of Bale et al. (2003) for the shock crossing on 2000-12-15/01:26:15, while panels (c) and (e) are similar to panels (b) and (d) but correspond to results from the present analysis. Panel (c) has to be compared with an enlarged view of panel (b) within the magnetosonic Mach number range $2 < M_{ms} < 6.5$. In panel (a), the transition of the density from upstream (unshocked) to downstream (shocked) states for a magnetosonic Mach number $M_{ms}=3.5$, $\theta_{Bn} = 81°$ shock (see text), where $M_{ms} =$

725 $V_{sw,sc}/c_{ms}$ with $c_{ms}= (c_s^2+ v_A^2)^{1/2}$, c_s is the sound speed, and $V_{sw,sc}$ is the bulk velocity of solar wind measured in the frame of the spacecraft; the green line is the hyperbolic tangent fit, and red vertical lines show the density transition scale. In panels (b) and (d), pink and green areas are superimposed to results of Bale et al. (2003) to indicate respectively the same M_{ms} range as for our study and another M_{ms} range (same width) for higher values for comparison. Panel (c) issued from present results shows the variation of the shock front thickness $L_{(ramp+ foot)}$ versus the M_{ms} range corresponding to the pink area defined in panel (b) where L is normalized to the ion inertial length c/ω_{pi} defined

730 upstream. Panel (e) issued from present results shows the variation of the shock front thickness $L_{(ramp+ foot)}$ versus M_{ms} for the same range, where L is normalized to $(v_{sh,n} /\Omega_{ci,2})$ in order to compare with panel (d), where $v_{sh,n}$ is the shock normal velocity defined in the frame of the solar wind and $\Omega_{ci,2}$ is the proton gyrofrequency defined downstream.

Krasnoselskikh et al. (2002)

735   Krasnoselskikh et al. (2002) have proposed another mechanism as a possible source of nonstationarity of the shock front (so called "gradient catastrophe"). In this mechanism, the transition to nonstationarity is characterized by the lack of the phase standing whistler wave train inside the shock front. This process takes place for oblique quasi-perpendicular shock (for a direction θ_{Bn} not too far from 90°) as the Alfven Mach M_A is above a certain critical Mach number given by $M_{nw} = (1/2)^{½}(M_i/m_e)^{½}\cos\theta_{Bn}$; this condition can be equivalently expressed for a fixed M_A as the direction θ_{Bn} is below a critical angular value.

740   In this case, the nonlinear steepening of the wave train cannot be balanced by the dispersion/dissipation effects. However, as mentioned in Sect. 1, this theoretical mechanism has strong limitations since (i) it is based on 1D model only and (ii) it excludes any dissipative effect. Indeed, reflected ions (which play a key role in supercritical Mach regime) are neglected and their impact on the shock dynamics – and in particular on the temporal fluctuations of the shock front micro-structures which is our center of interest in the present paper- is totally absent. Because of the above strong limitations, this process is still a source of

745   controversy.

Lobzin et al (2007)

Nevertheless, a further study made by Lobzin et al., (2007) has proposed the gradient catastrophe process as being at the origin of the shock front nonstationarity observed by Cluster on 24 January 2001. While the front nonstationarity is quite clear in the

750   experimental data which show quite different shock front profiles of the magnetic field crossed by the 4 satellites of Cluster, the proposed interpretation stays quite questionable for the following reasons: (i) the overall analysis is based on one shock crossing only (no statistical analysis has been performed), (ii) no procedure detailing the transfer from time to spatial scaling of the shock front (in particular focused separately on the ramp/foot structures) has been indicated so one ignores the percentages of errors underlying the spatial field profiles measurements which are not shown; (iii) no mapping and/or basic

755   information have been provided on the 3D disposal and inter-distance of the satellites, so that one ignores whether the four satellites cross the same shock front within the same or different successive self-reformation cycles; (iv) only one measurement of the ion density showing some fluctuations has been presented which is not enough for confirming that it could be due to the gradient catastrophe process. Moreover, note that such similar density fluctuations have been also measured quantitatively versus time in previous numerical simulations (Lembège and Savoini, 1992; Yang et al., 2009) but have been attributed as

760   being due to the self-reformation process fed by the accumulation of reflected ions and not to the gradient catastrophe process. Similar self-reformations have been also obtained as supported by the MTSI for an oblique propagating shock (Comisel et al., 2011); (v) a deeper analysis shows that the upstream ion temperature used in this paper is not the correct one since the CIS instrument was in magnetospheric mode (see Sect. 2) so that the moment calculations provide a large overestimate of the solar wind proton core temperature. Indeed, the determination of the upstream ion thermal velocity requires a delicate procedure

765   and is of central interest since the stationarity/nonstationarity of the shock front is strongly dependent on the ratio v_{sh}/v_{thi} (Schöler et al., 2003) or similarly on the ratio β_i (defined as the ion kinetic energy over magnetic energy) (Hada et al., 2003).

When using the solar proton temperature from the ACE satellite (4.5 eV thermal energy), the ion beta found is 0.6 instead of the value of 2.0 reported by Lobzin et al. (2007).

770 *Comisel et al (2011)*

The same data of Cluster measured on 24 January 2001 has been re-examined in detail by Comisel et al. (2011) and re-interpreted quite differently by using PIC simulations in plasma conditions and Mach number regimes chosen to be appropriate with experimental conditions. Basically, the authors have shown that the self-reformation is quite well recovered but is not controlled by the gradient catastrophe process (dispersive effects) mentioned above but rather by the self-reformation
775 mechanism fed up by the MTSI which is an indirect consequence of the ions reflection (dissipative effects which have been neglected in Krasnoselskikh et al. (2002)). Indeed, for slightly oblique shocks (out of 90°), the MTSI develops between the incoming electrons and incoming ions, with a growth rate large enough to develop during the gyration of the reflected ions (Schöler and Matsukiyo, 2004). These authors have shown that for a nonrealistic mass ratio, the self-reformation is still controlled by the collection of reflected ions at the upstream edge of the foot as in Lembège and Savoini (1992), since the
780 MTSI has a weak growth rate and has no impact on the nonstationary dynamics of the shock front. In contrast, for realistic mass ratio, the growth rate is much larger and MTSI can be easily excited which leads to ion phase mixing and thermalization. Then, the ion pressure increases considerably locally somewhere within the foot itself (and not at the edge of the foot) with associated building up and overtaking of the magnetic field. A new shock ramp builds up within the foot which initiates to reflect new incoming ions and a cyclic reformation is initialized. The cyclic period is lower than the one associated with the
785 self-reformation due to the accumulation of reflected ions (as in Lembège et Savoini, (1992)), since the process takes place before ions accomplish their full gyration. More precisely, by using the appropriate conditions of the 24th January 2001 shock crossing in the PIC simulations, Comisel et al. (2011) have shown that the waves triggered by this instability is of whistler type, have phase velocities directed downstream in the shock frame, and the associated Poynting flux (and wave group velocity) is also directed in the downstream direction. However, as these approach the density and magnetic field overshoot, the waves
790 are refracted; as a consequence, the Poynting flux changes direction and is directed upstream in the shock frame. In summary, there is no indication of a phase standing linear or nonlinear whistler precursor produced by the shock ramp itself in this process. This scenario does not support that proposed by Krasnoselskikh et al. (2002), where nonlinear whistler precursor is required to initialize the "gradient catastrophe" process as a source of the front nonstationarity.

795 *Hobara et al., 2010*

A statistical study based on 77 crossings of the terrestrial bow shock (30 by THEMIS and 47 by Cluster) have been performed by Hobara et al. (2010) in order to analyze the ramp scale and the associated gradient width. Their study claims that the spatial scale of the ramp decreases as the shock Alfven Mach number increases. However, detailed comparison with our results is difficult (almost impossible) at present time because of important missing information: (i) No detailed information is provided
800 on the procedure used for extracting the spatial widths of the ramp from the temporal experimental data as detailed in present

Sect. 2; (ii) the duration of the ramp crossing has been defined as a time interval between the upstream edge of the ramp and the maximum of overshoot. However, let us note that the upstream edge is not defined precisely (see the caution to account for in our Section 3) and the use of the overshoot can lead to an overestimate of the ramp width as compared to the method used herein (Sect. 3) since it is partially polluted by reflected ions; (iii) statistical errors are indicated in their Figures 2 and 3

805   only for range of Mach numbers and not on individual measurements; (iv) no statistics are shown versus the direction θ_{Bn} of the shock front normal; as a consequence, one ignores how/whether the measurements of the ramp /foot bounds are polluted by the whistler (either linear either nonlinear) whose emission strongly depends on the angle θ_{Bn}; (v) no statistics/information are indicated on the ion β_i value (which has a strong impact on the shock front self-reformation) (Hada et al., 2003); (vi) the authors use two different statistics: one based on the ramp spatial scale (their Figure 2), the other based on magnetic ramp

810   spatial gradient scale (their Figure 3). Moreover, they used a simple theoretical argument (based on dispersive whistler) to stress that the wavelength L_w of the linear/nonlinear whistler varies as $L_w \sim 1 / M_A$. But, the fact that both statistics show that the width of the measured structure decreases as M_A increases does not imply that dispersion determines the size of the magnetic ramp even for supercritical shocks (as discussed later on); (vii) at least, only a very limited number of measurements (whatever the M_A value is within the concerned range M_A=2-12 in Hobara et al., 2010) indicates that the ramp width succeeds to reach a

815   few electron inertial lengths (equal or lower than 5 $\tilde{c}/\tilde{\omega}_{pe}$, in their Figures 2 and 3) which is in strong contrast with our statistical results of Figure 8a. The lack on statistics versus θ_{Bn} and β_i (above points (iv) and (v)) and the absence of precise information on the methodology used in the statistics of Hobara et al. (2010) (as listed above) could explain this difference.

Moreover, Hobara et al. (2010) deduce that their measurements (in particular the decrease of the ramp thickness as M_A increases) evidence that the major process responsible for the shock front nonstationarity is the "gradient catastrophe" process

820   proposed by Krassnoselskikh et al. (2002), and Lobzin et al. (2007). However, three main facts contradict this statement: (i) arguments describing the limitations of the theoretical model (Krassnoselskikh et al., 2002), and the revised analysis of Comisel et al. (2011) as already described above in present section, (ii) Hobara et al. (2010) use the overshoot (observed in the set of their experimental measurement) as an upper bound to define the ramp width; but the overshoot of supercritical shocks is a clear signature of the reflected ions as these gyrate downstream after being once reflected at the ramp (Leroy et al., 1982).

825   Then, a contradiction occurs since dissipation effects (strongly carried by the reflected ions) have been fully neglected in the model of "gradient catastrophe" which cannot support their statements; (iii) a similar variation of the ramp thickness as M_A increases has been also observed in the self-reformation process in PIC simulations (not shown here), which means that this variation cannot be used as a unique signature of the "gradient catastrophe" process. At least, in order to support their statements, Hobara et al. (2010) remind that PIC simulations evidencing the self-reformation due to the accumulation of

830   reflected ions at a foot distance from the ramp (as in Lembège and Savoini, (1992)) as well as due to the MTSI (as in Matsukyio and Schöler, (2006) use low ω_{pe}/ω_{ce} ratio, which overestimates the electric field to magnetic field ratio (in practice, using a realistic ω_{pe}/ω_{ce} ratio is very difficult at present time for computational constraints). If were true, this argument would suggest that the electric field would be too large and that the self-reformation process would result from an artefact. However, no

quantitative result has been obtained until now to support such a statement. In contrast, let us remind that (i) the parametric

835 analysis performed by Lembège et al. (2009) clearly evidences that both hybrid and PIC simulation retrieve the same self-

reformation process of the shock front in similar plasma conditions and Mach regime, provided that the space grid is small

enough (i.e. high resolution) in hybrid simulations as shown initially by Hellinger et al. (2002); this last result would suggest

that the field gradients at the ramp are important and not the absolute fields amplitude; (ii) electron scales are neglected in

common hybrid simulations (as those used in Hellinger et al., (2007); Lembège et al., (2009) and references therein) which are

840 independent of the ratio ω_{pe}/ω_{ce}. This suggests that the ratio ω_{pe}/ω_{ce} has no direct impact on the self-reformation. Note, that the

ramp width may be estimated in terms of percentages of ion inertial length in hybrid simulations and both in terms of electron

and ion inertial lengths in PIC simulations.

In summary, the measurements of Hobara et al. (2010) do not support the model describing the ramp as an evolving

nonlinear whistler wave, neither the mechanism of "gradient catastrophe" process of Krassnoselskikh et al. (2002) as a source

845 of the front nonstationarity.

Schwartz et al. (2011)

Schwartz et al. (2011) have determined the scale of the electron temperature gradient via electron distributions measured in

situ by the Cluster spacecraft and have identified two different scales; the Mach number is supercritical ($M_A=3.8$) and the

850 shock propagation is oblique ($\theta_{Bn} =83°$). First, the authors found that half of the electron heating coincides with a narrow layer

covering several electron inertia lengths (c/ω_{pe}) and found an inflated electron distribution due to primarily the electron filling

in/or the entrapment in regions of phase space that would be not accessible. Second, the remaining of the solar wind maximum

is only present in the smoother increase of the field which precedes the ramp; this beam is totally destroyed by the time this

electron scale ramp is crossed. The authors found that this scale is comparable to that deduced from the theoretical limiting

855 case of a wave capable of phase standing in the incident flow and concluded that this suggests that supercritical shocks steepen

to this whistler limit since dissipation processes are insufficient to broaden the transition further.

However, several elements of information are missing: (i) the authors mentioned to have used a technique to convert

the time series of data to distance along the shock normal similar to that of Schwartz (1998) i.e. the procedure to determine the

normal and the velocity of the shock from multi-spacecraft measurements (as in Sect. 2) but did not provide detailed

860 information on the procedure itself, associated errors estimate, or on the definition of the ramp itself (their Figure 1); (ii) the

results are limited to one shock crossing (one spacecraft only); some attempts to other shock crossings are mentioned but no

statistical results have been shown or summarized; (iii) the observed results cannot lead to the conclusions that dissipation

processes are insufficient to broaden the transition further, since once again the key dissipation processes driven by the

(reflected) ions are not mentioned /analysed in this study. Of course, dispersive effects must be considered in the global balance

865 of nonlinear steepening of the front by both dispersive/dissipative effects, but this does not mean that the shock front dynamics

is controlled by dispersive effects. Moreover, other sources of fields fluctuations may take place in the shock front (such as

formation of multi-peaks (signatures of old/new self-reformation (Sec. 4.4.2), and/or whistler waves excited by the MTSI within the front) without invoking any dispersive effect.

5.2 Spatial measurements of the substructures

870 Walker et al. (2004) investigated short scale structures in the electric field that are observed during crossings of the quasi-perpendicular bow shock using also data from the Cluster satellites. An example is reproduced from this paper on Figure 12a. The structures observed at each Cluster satellite magnetic front exhibit large amplitudes, as high as 70mV/m and the authors argue they make a significant contribution to the overall change in potential at the shock front. They have shown that the scale size of these short-lived electric field structures is of the order of a few c/ω_{pe} as shown on their statistics reproduced in Figure

875 12c. They also studied the relationships between the scale size and the upstream Mach number and θ_{Bn}. They found that the scale size of these structures decreases with increasing plasma β_i and as $\theta_{Bn} \sim 90°$.
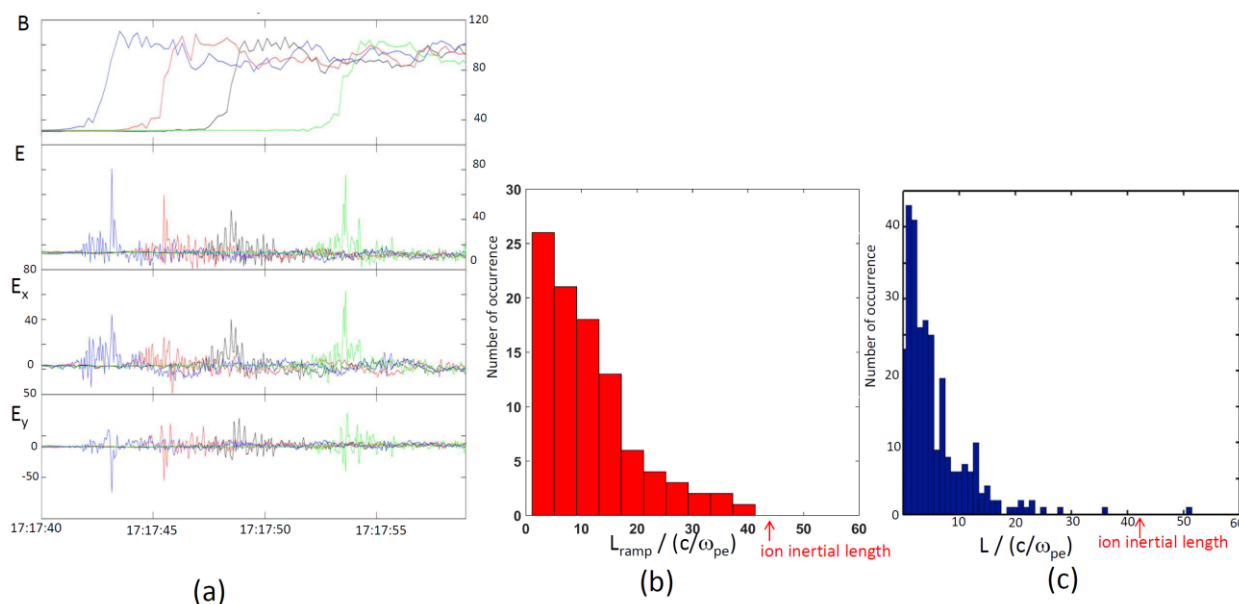
Figure 12: Panels (a) and (c) are reproduced from Walker et al. (2004). Panel (a) displays an example of short scale electric field structures
880 observed around the crossing of the bow shock by the Cluster quartet on March 31, 2001 at 1718 UT (first panel: spin time resolution magnetic field magnitude; following panels display the amplitude of the electric field and E_x and E_y GSE components, respectively). Panel (b) reproduces the distribution of magnetic field ramp obtained from the present study already shown in Figure 8a to compare with the distribution of the electric field structures of Walker et al. (2004) shown on panel (c).

885 Interestingly, the comparison of distributions displayed on Figure 12b (present analysis) and Figure 12c (Walker et al., 2004) shows that the electric field structures are consistent with substructures of the ramp since the typical scales found seem smaller. Of course, to be fully conclusive, one would need to compare the size of the electric field structure and of the magnetic ramp

for each shock crossing. However, both results seem very consistent. Recently, Dimmock et al. (2019) has evidenced electron-scale field structures inside the shock ramp from a case study using the observations of only two Cluster spacecraft which were
890   very close to each other and proposed that it is associated to the transition to nonstationarity.

5.3 Spatial measurements of the foot thickness

As compared with studies focused on the ramp width, previous works dedicated to the spatial measurements of the foot thickness are in relatively limited number. First observations of the foot have been made by Paul et al. (1965). Woods (1969; 1971) has proposed the reflected ions to account the foot structure and has estimated a foot width for a strictly perpendicular
895   shock from the turning point distance (Eq. 4 of Sect. 4.3 which is recalled here):

$L_{\text{foot}} = 0.68\,\rho_{\text{ci,sw}}$ (4)

assuming a specular reflection of ions, where $\rho_{\text{ci,sw}}$ is the upstream ion gyradius estimated from the bulk velocity of the solar wind (and not from the ion thermal velocity); the reflection is specular in the sense that the incident ion's velocity component along the shock normal is reversed at the shock, while the component perpendicular to the shock normal remains unchanged.
900   A good agreement has been found with ISEE 1 & 2 data by Paschman et al., (1982), and Sckopke et al., (1983). However, two points need to be stressed out: (i) the measurement has been made from the ramp to the turning out point of reflected ions for five ISEE 1 & 2 crossings of the shock (the thickness of the foot should be comparable to this turnaround distance), (ii) the condition of specular reflection is not simple when applied to oblique shocks, as shown by Livesey et al. (1984) who have extended the turning distance to ion reflection with an arbitrary direction θ_{Bn} of the shock normal, and estimated the foot
905   thickness as in Eq. (3) of Sect. 4.3 we recall here:

$d = 0.68\,\rho_{ci}\cos\theta_{vn}\,\sin^2\theta_{Bn}$ (3)

where θ_{Vn} is the acute angle defined between the incoming solar wind direction and the normal to the shock front. A good agreement has been obtained between the experimental measurements (distance from the ramp and to the turning point of reflected ions for several shock crossings made by ISEE 1 & 2) and values deduced from Eq. (1). Moreover, Moses et al.
910   (1985) found that the shock velocity v_{sh} in the frame of the spacecraft can be expressed as:

$v_{sh} = v_{SW}\,(x\,/\,(1+\text{ or }-x))$

where

$x = 0.68\,\rho_{\text{ci,us}}\cos(\theta_{Vn})\,\sin^2(\theta_{Bn})/\,\Omega_{\text{ci}}\,\Delta t$ (5)

"-" sign refers to a transition from upstream to downstream, the "+" sign refers to the inverted transition, Ω_{ci} is the upstream
915   ion gyrofrequency and Δt is the foot traversal time. Later on, Gosling and Thomsen (1985) have derived a more general expression for the turnaround distance $d_{turning}$ for arbitrary θ_{Bn} which differs from (3) particularly for $\theta_{Bn} < 60°$, and which incorporates above Eq. (1) and (2) of Sect. 4.3. Initial steps of their derivation of $d_{turning}$ are closely similar to the formalism initially developed by Schwartz et al. (1983) and leads to (Gosling and Robson, 1985):

$d_{turning} = \rho_{\text{ci,sw}}\;\cos(\theta_{Vn})\,F(\theta_{Bn})$ (6)

920   where:

$$F(\theta_{Bn}) = \Omega_{ci}\, t_1\, (2\,\cos^2(\theta_{Bn}) - 1) + 2\,\sin^2(\theta_{Bn})\,\sin(\Omega_{ci}\, t_1) \tag{7}$$

with $\cos(\Omega_{ci}\, t_1) = (1 - 2\,\cos^2(\theta_{Bn})) / 2\,\sin^2(\theta_{Bn})$ (8)

and t_1 is the time of the turnaround defined by $dx_n/dt = 0$, where x_n is the coordinate of the ion along the normal.

Results obtained by Eq. (3) and (6) - (8) have been compared and analyzed by Gosling and Thomsen (1985).

925   Since present statistics concern quasi-perpendicular shock with shock normal direction range $74° < \theta_{Bn} < 90°$ (Figures 8 et 9),

one can apply and compare Eq. (6) – (8) to our statistical results. Above Eq. (3) to (8) have been obtained within the frame of

a stationary foot where the overall shock front profile (composed with ramp and foot) is fixed. Values obtained from Eq. (6) -

(8) have been reported in Figure 9b (red dots), where each value includes the dependence of θ_{Bn} for each shock crossing. Then,

results of Figure 9b confirm well that Eq. (6) - (8) provide an upper bound of the foot thickness for all experimental

930   measurements analyzed herein. Indeed, the conditions for ions reflection are varying in time. Numerical simulations have

already shown that: (i) the density of reflected ions cyclically varies with a period equal to the self-reformation cycle (formation

of ions bursts as shown in previous works (Lembège and Savoini, 1992; Yang et al., 2009; Comisel et al., 2011); similarly,

bursts of electron (with parallel kinetic energy) are formed for oblique shocks as long as the self-reformation persists for

oblique shock until a certain critical angle (Lembège and Savoini, 2002); (ii) the shock front variability has also a strong impact

935   on the nature of the acceleration process SSA (shock surfing acceleration) versus SDA (shock drift acceleration) during their

reflection as shown by Yang et al. (2009).

In the same way, a super-upper bound value of the foot thickness can be obtained from the simplified Eq. 3 defined for a

strictly perpendicular shock. The deduced value $L_{foot}/\rho_{ci,us} = 0.68$ (herein the convection bulk velocity of the solar wind is equal

to the shock velocity since we are in the rest solar wind reference frame) has been reported in simulation results of Figure 10d

940   (perpendicular shock). Eq. 3 provides a very good upper limit of the time variation of the foot thickness.

In summary, since the shock front is highly nonstationary, no fixed theoretical scale can be provided as a reference in

contrast with statements of many previous works. Present results confirm that considering the whole shock front to determine

the transition layer width can be a source of errors and misunderstanding. Instead, (i) a detailed and separate analysis of

microstructures (ramp, foot -and later overshoot-) is necessary, and (ii) a comparison with a lower bound value (for the ramp

945   width) and upper bound value (for the foot width) reveals to have a full meaning.

6 Conclusions

6.1 About the methodology used for extracting the spatial width of each fine structure:

i) this works presents in detail the different steps necessary to determine carefully and without ambiguity the spatial thicknesses

of each fine structure from the magnetic field measurements which are summarized as follows:

950   -   First, an upstream time interval is defined in the time series for each of the four spacecraft and an average magnetic field is determined. If all average fields agree in direction and magnitude within predefined limits, an unperturbed upstream field $\mathbf{B_0}$ is obtained for the global shock crossing by the four satellites;

    -    Second, for each spacecraft, the entry times in the magnetic foot are automatically determined when the values of the components and magnitude exceed the upstream values by a certain value defined from the upstream standard deviations; then

955 one validates by visual inspection that results are not polluted by any upstream disturbance or detached wave packet.

    -    Third, a downstream interval is defined to measure the downstream asymptotic value of the magnetic B field magnitude.

    -    Fourth, for each spacecraft, an automatic procedure is applied on the magnitude of the magnetic field to determine the entry in an exit times from the magnetic ramp. This procedure is initialized by preliminary estimates using the upstream

960 and downstream asymptotic levels and based on a linear regression used only to better define the time interval where the gradient is the strongest with the best correlation coefficient;

    -    Fifth, the exit time from the first overshoot is estimated first by the magnetic field magnitude reaching the downstream asymptotic value for the closest time to the first undershoot and then adjusted by allowing a reasonable variation (for instance 5%) of the downstream asymptotic value (see Sect. 2, Fig. 2a);

965   -   Sixth, the interval variations of the entry/exit times for each microstructure are used to define error bars on them;

    -    Seventh, the values of both the normal to the shock and its velocity in each spacecraft frame is determined using the four-spacecraft timing method. The obtained normal vector $\mathbf{n_0}$ is then used to determine the general geometry of the shock characterized by the angle θ_{Bn0} with the unperturbed upstream field vector $\mathbf{B_0}$ determined above. The error bars on θ_{Bn0} comes from both the determination of $\mathbf{B_0}$ and $\mathbf{n_0}$ from the timing errors;

970   -   Eighth, the spatial profile along the normal direction $\mathbf{n_0}$ is derived for each spacecraft in units of upstream ion inertial length and the microstructure thicknesses are derived in terms of appropriate physical lengths.

ii) the fitting technics based on exponential or hyperbolic function and used in previous works to match to match a shock front profile is questionable since these lead to mixing spatial scales of the foot and the ramp. Rather, our statistical results state that a linear best fit with appropriate identification of the upper and lower bounds of the temporal time ranges of the ramp and the

975 foot is much more accurate and allows a precise error estimate on the spatial width of each microstructure.

6.2 About comparing experimental with numerical simulation/theoretical results:

Simulation of a strictly perpendicular case as presented in Sect. 4 can be considered herein as a reference case allowing to provide some bounds range within which statistics of experimental results may be inserted. More precisely, these provide the following information: the time variation of the ramp thickness is relatively limited (almost constant) and one can define a

980 'lower limit' (a few electron inertial lengths) for the ramp width. In contrast, the foot thickness is strongly varying in time and one can define an 'upper limit' provided by Eq. 2 (which simplifies into Eq. 3 for a strictly perpendicular shock).

Moreover, statistical analysis of measurements appear to be much more essential than the analysis of a single shock crossing only, in order to gather relevant information on the widths of the front microstructures. Since no shock crossing will be exactly identical one to each other even after a deep selection of data, we have to collect several shock crossings in slightly
985 different conditions in terms of Mach number regime, of shock normal direction, of β_i plasma conditions and of orientation of the shock crossing by the 4 satellites set. In addition, each shock crossing reveals some variability of fine structures thickness within the front. Then, no one to one correspondence in comparing numerical and experimental data for each crossing is possible; instead, the use of 'lower' and 'upper' limits mentioned above reveals to have a full meaning.

6.3 About the possible identification of the process responsible for the shock front nonstationary:

990 Several points need to be emphasized:

(i) All shocks profiles analysed herein exhibit a foot and overshoot which are clear signatures (in supercritical regime) of the gyration of reflected ions upstream of the ramp, and of these same reflected ions which succeed to penetrate downstream after being once reflected at the ramp. Then, dissipation effects carried by these reflected ions need to be fully considered. Among the different mechanisms proposed to account for the shock front nonstationary, only two processes named 'self-
995 reformation' include self consistently (without any approximation) the competition between the nonlinear, dissipative and dispersive effects, and in particular the important role of reflected ions on the shock dynamics (and vice versa). Up to now, one still ignores whether the self-reformation is mainly controlled by the accumulation of reflected ions which is observed for perpendicular and quasi-perpendicular shocks (Lembège et Savoini, 1992) or by the MTSI-1/MTSI-2 (Schöler and Matsukyio, 2004: Muschietti and Lembège , 2017) which is triggered only for oblique shocks (out of 90°); MTSI-1 and MTSI-2 refer to
1000 the instability excited in the foot region by the relative drift between the reflected ions/incoming electrons and the incoming ions/incoming electrons respectively. This open question will require a further analysis which is under investigation.

(ii) Among others, one typical signature of a front self-reformation is the anticorrelation between the time variation of the 'new' growing foot and the 'old' overshoot as illustrated in Figure 10a. Indeed, as the amplitude of the new foot increases, new incoming ions start to be reflected, which has an impact in the need for local dissipation at the overshoot located just
1005 behind. Then, a clear identification of a given self-reformation process would require an inter-satellites distance such that the four satellites cross the same shock front within its same reformation cycle. This requires a short inter-satellites distance for the quartet. This seems more easily addressed with the Magnetospheric MultiScale (MMS) mission data though the spacecraft separation is so small that low-scale fluctuations of the shock front (ripples) has a different impact on the normal determination. These low-scale ripples have been identified in a single-case study by Johlander et al. (2016) and also indicated from the
1010 observed variations of the cross-shock potential in another single-case study by Hanson et al. (2019).

(iii) We emphasize the importance of dimensionality effects in simulations studies for identifying what mechanisms can be dominant in the shock front nonstationarity. For a strictly perpendicular propagating shock, both 2D hybrid and PIC simulations have clearly evidenced the emission of nonlinear whistler waves which stay stationary with the ramp, and propagate obliquely with respect to both the shock normal and the upstream magnetostatic field B_o (Lembège and al., 2009;

1015 Hellinger et al., 2007). This emission holds only as the B_o field is laying within the simulation plane (and self-reformation is absent) and disappears as B_o is out of the simulation plane (and self-reformation is present). The source of this whistler emission has not been clearly confirmed yet; ion Weibel instability has been recently proposed as a possible mechanism (Burgess et al., 2016). In other words, the emission of these whistlers seems to be associated with the disappearance of any self-reformation process. But, this enigmatic observation reveals that 3D PIC simulation is necessary in which the B_o field is
1020 fully involved whatever its orientation is in the simulation box. Preliminary results of Shinohara et al. (2007) based on 3D PIC simulations show that both processes (emission of nonlinear whistler from the ramp and front self-reformation) can co-exist. In other words, the time variation of the ramp/foot thickness associated to the self-reformation should persist in 3D simulation; a further quantitative study is also required in order to check the scales of the front microstructures.

Acknowledgments

1025 Thanks are addressed to the International Space Science Institute (Bern Switzerland), the National PNST program of CNRS (Centre National de la Recherche Scientifique) for their support. BL also acknowledges the French Centre National d'Etudes Spatiales (CNES) for its support under APR- W-EEXP/10-01-01-05 and APR-Z-ETP-E-0010/01-01-05. BL thanks IDRIS national computer center (located at Orsay, near Paris) where present results issued from numerical simulations have been obtained, for its support (DARI project A0050400295). The Cluster data come from the ESA archive data center:
1030 https://www.cosmos.esa.int/web/csa.

References

Bale, S.D., et al. (2003), Density-transition scale at quasiperpendicular collisionless shocks, Phys. Rev. Lett., DOI: 10.1103/PhysRevLett.91.265004.

Bale, S. D., et al. (2005), Quasi-perpendicular Shock Structure and Processes, Space Science Reviews, v. 118, Issue 1-4, pp.
1035   161-203.

Balogh A., C. M. Carr, M. H. Acuña, M. W. Dunlop, T. J. Beek , P. Brown, K.-H. Fornacon, E. Georgescu, K.-H. Glassmeier, J. Harris , G. Musmann , T. Oddy , and K. Schwingenschuh (2001), The Cluster Magnetic Field Investigation: overview of in-flight performance and initial results, Annales Geophysicae,19: 1207–1217.

Balikhin, M., et al. (1995), The Scales in Quasi-perpendicular Shocks, Adv. Space Res. Vol. IS, No. 819, pp. (8/9)247-
1040   (8/9)260.

Biskamp, B. and Welter, H. (1972), Numerical Studies of Magnetosonic Collisionless Shock Waves, Nuclear Fusion. 12, 663.

Burgess, D., W. P. Wilkinson, and S. J. Schwartz (1999), Ion distributions and thermalization at perpendicular and quasi-perpendicular supercritical collisionless shocks, J. Geophys. Res., 94, 8783–8792.

Burgess, D., Hellinger, P., Gingell, I., and Trávnícek, P.M. (2016), Microstructure in two- and three-dimensional hybrid
1045   simulations of perpendicular collisionless shocks, J. Plasma Phys., vol. 82, 905820401,
        doi:10.1017/S0022377816000660.

Burlaga, L. F. (1971), On the nature and origin of directional discontinuities, J. Geophys. Res., 76, 4360.

Chapman, S. C., R. E. Lee, and R. O. Dendy (2005), Perpendicular shock reformation and ion acceleration, Space Sci. Rev.,
        121.

1050   Comisel H., M. Schöler , J. Soucek , and S. Matsukiyo (2011), Non-stationarity of the quasi-perpendicular bow shock:
        comparison between Cluster observations and simulations, Ann. Geophys., 29, 263–274, 2011, doi:10.5194/angeo-29-
        263.

Dimmock, A. P., C. T. Russell, R. Z. Sagdeev, V. Krasnoselskikh, S. N. Walker, C. Carr, et al. (2019), Direct evidence of
        nonstationary collisionless shocks in space plasmas, Sci. Adv. 5, eaau9926, doi: 10.1126/sciadv.aau9926.

1055   Escoubet, C. P., Masson, A., Laakso, H., and Goldstein, M. L. (2015), Recent highlights from Cluster, the first 3-D
        magnetospheric mission, Ann. Geophys., 33, 1221-1235, doi:10.5194/angeo-33-1221-2015.

Forslund, D. W., Quest, K. B., Brackbill, J. U. and Lee, K. (1984), Collisionless dissipation in quasi-perpendicular shocks, J.
        Geophys. Res., 89, 2142.

Galeev, A.A., V. Krasnoselskikh and V. Lobzin (1999), Fine structure of a quasi-perpendicular supercritical shock wave,
1060   Soviet J. Plasma Physics, 15,697.

Gosling J.T. and M. F. Thomsen (1985), Specularly reflected ions, shock foot thicknesses, and shock velocity
        determinations, J. Geophys. Res., vol. 90, A10, 9893-9896.

Gosling J.T. and A.E. Robson (1985), Ion reflection, gyration and dissipation at supercritical shocks, in Collisionless Shocks
        in the Heliosphere: Reviews of Current Research, ed. B.T. Tsurutani and R.G. Stone, Copyright by the American
1065   Geophysical Union.

Greenstadt, E.W., PC. Hedgecock, and C.T. Russell (1972), Large-Scale Coherence and High velocities of the Earth's bow
        shock on February 12,1969, J. Geophys. Res., 22, 1116.

Greenstadt, E.W., V. Formisano, C.T. Russell, FL. Scarf, and M. Neugebauer (1975), Structure of the quasiperpendicular
        laminar bow shock, J. Geophys. Res., 80,502.

1070   Hada, T., M. Oonishi, B. Lembège, and P. Savoini (2003), Shock front nonstationarity of supercritical perpendicular shocks,
        J. Geophys. Res., 108 (doi:10.1029/2002JA009339), 3–1.

Hanson, E. L. M., Agapitov, O. V., Mozer, F. S., Krasnoselskikh, V., Bale, S. D., Avanov, L., et al. (2019). Cross-shock
        potential in rippled versus planar quasi-perpendicular shocks observed by MMS. Geophysical Research Letters, 46, 2381–
        2389. https://doi.org/10.1029/2018GL080240.

1075   Hellinger P. and P. Travnicek and H. H. Matsumoto (2002), Reformation of perpendicular shocks: Hybrid simulations,
        Geophys. Res. Lett., vol. 29, no. 24, 2234, doi:10.1029/2002gl015915.

Hellinger P., P. Travnicek, B. Lembège, and P. Savoini (2007), Emission of nonlinear whistler waves at the front of perpendicular supercritical shocks: Hybrid versus full particle simulations, Geophys. Res. Lett., vol. 34, 114109, doi:10.1029/2007gl030239.

1080   Heppner, J.P., Sigura, T., B.G L. Skillman. Ledley, and M. Campbell (1967), OGO-A magnetic field observations, J. Geophys. Res., 22.54 17.

Hobara Y., M. Balikhin, V. Krasnoselskikh, M. Gedalin and H. Yamagishi (2010), Statistical study of the quasi-perpendicular shock ramp widths, J. Geophys. Res., 115, A11106, doi:10.1029/2010JA015659

Holzer, R.E., M.G. McLeod, and E.J. Smith (1966), Preliminary results from OGO-1 Search Coil Magnetometer: Boundary
1085   Positions and Magnetic Noise Spectra, J. Geophys. Res., a, 148l.

Horbury T.S., P. J. Cargill, E. A. Lucek, A. Balogh, M.W. Dunlop, T. M. Oddy, C. Carr, P. Brown, A. Szabo, and K.-H. Fornacon (2001), Cluster magnetic field observations of the bowshock: Orientation, motion and structure, Annales Geophysicae, 19: 1399–1409.

Horbury T.S., P. J. Cargill, E. A. Lucek, J. Eastwood, A. Balogh, M. W. Dunlop, K.-H. Fornacon and E. Georgescu (2002),
1090   Four spacecraft measurements of the quasiperpendicular terrestrial bow shock: Orientation and motion, J. Geophys. Res., Vol. 107, A8, 10.1029/2001ja000273.

Johlander, A., Schwartz, S. J., Vaivads, A., Khotyaintsev, Y. V., Gingell, I., Peng, I. B., et al. (2016). Rippled quasiperpendicular shock observed by the Magnetospheric Multiscale spacecraft. Physical Review Letters, 117(16), 165101. https://doi.org/10.1103/PhysRevLett.117.165101.

1095   Kaufmann, R.L. (1967), Shock observation with the explorer 12 Magnetometer, J. Geophys. Rex, 72, 9.

Krasnoselskikh, V.V., B. Lembège, P. Savoini et V.V. Lobzin (2002), Nonstationarity of Strong Collisionless Quasi-Perpendicular Shocks: Theory Versus Full Particle Numerical Simulations, Phys. Plasmas 9(4), 1192.

Lefebvre, B., Y. Seki, S. J. Schwartz, C. Mazelle, and E. A. Lucek (2009), Reformation of an oblique shock observed by Cluster, J. Geophys. Res., vol. 114, a11107, doi:10.1029/2009ja014268.

1100   Lembège B. and J.M. Dawson (1987), Self-consistent study of a perpendicular collisionless and nonresistive shock, Phys. Fluids, 30, 6.

Lembège B. and J.M. Dawson (1989), Formation of double layers within an oblique collisionless shocks, Phys Rev Letters, 62, 2683-2686.

Lembège, B., Walker, S. N., Savoini, P. and Krasnoselskikh, V. (1999), 'The spatial sizes of electric and magnetic field
1105   gradients in a simulated shock', Adv. Space Rev., 24, 1, 109.

Lembège, B., J. Giacalone, M. Schöler, T. Hada, M. Hoshino, V. Krasnoselskikh, H. Kucharek, P. Savoini, and T. Terasawa (2004), Selected problems in collisionless shocks Physics (review), Space Science Rev., 110: 161-226.

Lembège B. and P. Savoini (1992), Nonstationarity of a two-dimensional quasiperpendicular supercritical collisionless shock by self-reformation, Phys. Fluids, 4, 11.

1110 Lembège B., Z. Huang, P. Martel, and D.S. Cai (2008), Analysis of Collisionless Shock Turbulence by Using Virtual Satellites in 2-D Full Particle-in-Cell Simulations, IEEE Transactions on Plasma Science, Vol. 36, No. 4, p. 1172-1173.

Lembège B. and P. Savoini (2002), Formation of reflected electron bursts by the nonstationarity and nonuniformity of a collisionless shock front, Journal of Geophysical Research, vol. 107, no. a3, 1037, 10.1029/2001ja900128.

Lembège B., Z. W. Yang and Q. Lu (2013a), Variability of the shock front of a perpendicular supercritical shock when
1115   approaching realistic conditions: impact on the self-reformation process, EGU2013 meeting, ST1.3-7294.

Lembège B., Z. W. Yang and Q. Lu (2013b), Impact of the plasma realistic conditions approach on the macroscopic fields features at a perpendicular supercritical shock front, AGU2013 fall meeting, 1801714, SM31A-2112.

Lembège B., P. Savoini, P. Hellinger and P.M. Travnicek (2009), Nonstationarity of a two-dimensional perpendicular shock: Competing mechanisms, J. Geophys. Res. vol. 114, a03217, doi:10.1029/2008ja013618.

1120 Leroy M.M., D. Winske, C.C. Goodrich, C.S. Wu, and K. Papadopoulos (1982), The Structure of Perpendicular Bow Shocks, J. Geophys. Res., Vol. 87, No. a7, 5081-5094.

Livesey W.A., C. F. Kennel, and C. T. Russell (1982), ISEE-1 and -2 observations of magnetic field strength overshoots in quasi-perpendicular bow shocks, Geophys. Res. Lett., vol. 9, no. 9, pages 1037-1040.

Livesey W.A., C. T. Russell, and C. F. Kennel (1984), A comparison of specularly reflected gyrating ion orbits with observed
1125   shock foot thicknesses, J. Geophys. Res., 89, No. a8, p. 6824-6828.

Lobzin,V. V., et al. (2007), Nonstationarity and Reformation of High-Mach Number Shocks: Cluster Observations, Geophys. Res. Lett., v. 34, L05107.

Lobzin, V.V., et al. (2008), On nonstationarity and rippling of the quasiperpendicular zone of the Earth bow shock: Cluster observations, Annales Geophysicae, 26, 2899–2910.

1130 Marcowith A., A. Bret, A. Bykov, M.E. Dieckman, L.O.C Drury, B. Lembège, M. Lemone, G. Morlino, G. Murphy, G. Pelletier, I. Plotnikov, B. Revillle, M. Riquelme, L. Sironi and A.Stockem Novo, (2016), The microphysics of collisionless shock waves , Report of Progress in Physics, IOP Publishing, 79, 046901

Matsukyio T. and M. Schöler (2003), Modified two-stream instability in the foot of high Mach number quasi-perpendicular shocks, J. Geophys. Res., 108, A12, 1459, doi:10.1029/2003ja010080.

1135 Mazelle., C., B. Lembège, A. Morgenthaler, K. Meziane, T. Horbury, E.A. Luce, I. Dandouras (2007), Evidence of quasi perpendicular shock front nonstationarity from Cluster data: comparative approach with numerical simulation results, *Eos Trans. AGU*, 88(52), Fall Meet. Suppl., Abstract # SM11A-0309.

Mazelle, C., Lembège, B., Morgenthaler, A., Meziane, K., Horbury, T., Lucek, E.A., Dandouras, I. (2008a), Nonstationarity of quasi-perpendicular shock front: comparative approach from Cluster data with numerical simulation results, Vol. 10,
1140   EGU General Assembly, EGU2008-A-09809, Id: 1607-7962.

Mazelle, C., B Lembège, K Meziane, J Rauch, J Trotignon, E Lucek, and I. Dandouras (2008b), Evidence of the self-reformation of the quasi-perpendicular terrestrial shock front from Cluster data, *Eos Trans. AGU*, 89(53), Fall Meet. Suppl., Abstract # SM51A-1618.

Mazelle, C., B. Lembège, A. Morgenthaler, K. Meziane, T. S. Horbury, V. Genot, E. A. Lucek, and I. Dandouras (2010), Self-reformation of the quasi-perpendicular shock: Cluster observations, Twelfth International Solar Wind Conference, AIP Conf. Proc., 1216; 471, doi:10.1063/1.3395905.

Mazelle, C., B. Lembège, A. Morgenthaler, K. Meziane (2010), "Nonstationarity of quasi-perpendicular shocks: magnetic structure, ion properties and microturbulence", SM01. SPA-Magnetospheric Physics, AGU Fall meeting, *Eos Trans. AGU*, 91(55), Fall Meet. Suppl., Abstract # SM51B-1792, 2010.

Mazelle, C., B. Lembège and A. Morgenthaler (2011), Evidence of Micro-turbulence and nonstationarity at Quasi-Perpendicular Shocks: Cluster results, SM14 Revelations from Multipoint Measurement: Space Plasma Processes and Dynamics, AGU Fall meeting, *Eos Trans. AGU*, 92(56), Fall Meet. Suppl., Abstract # SM51B-2075.

Mazelle, C., B. Lembège, et K. Meziane (2012), Nonstationary dynamics of collisionless shock front : Influence on particle reflection and acceleration, Fall Meeting, San Fransisco, SH32B-03, Id : 1488970.

Mellott M.M. et W.A. Livesey (1987), Shock Overshoots, J. Geophys. Res., Vol. 92 (a12), 13.661.

Meziane, K., T. Y. Alrefay, and A. M. Hamza (2014), On the shape and motion of the Earth's bow shock, Planet. Space. Sci., 93-94, pp1-9, doi:10.1016/j.pss.2014.01.006.

Meziane, K., A. M. Hamza, M. Maksmovic and T. Y. Alrefay (2015), The Earth's bow shock velocity distribution function, J. Geophys. Res., 120, 1229-1237, doi:10.1002/2014JA020772.

Moses, S.L, F.V Coroniti, C.F. Kennel, F. L. Scarf, E.W. Greenstadt , W.S. Kurth , and R.P. Lepping (1985), High time resolution plasma wave and magnetic field observations of the Jovian bow shock, Geophys. Res. Lett., 12 (4), 183.

Moullard, O., D. Burgess, T. S. Horbury, and E. A. Lucek (2006), Ripples observed on the surface of the Earth's quasi-perpendicular bow shock, J. Geophys. Res., Vol. 111, a09113, doi:10.1029/2005ja011594.

Muschietti, L. and B. Lembège (2006), Electron cyclotron microinstability in the foot of a perpendicular shock: A self-consistent PIC simulation, Adv. Space Res., 37, 483–493, doi:10.1016/j.asr.2005.03.077.

Muschietti L. and B. Lembège (2013), Microturbulence in the electron cyclotron frequency range at perpendicular supercritical shocks, J. Geophys. Res.: Space Physics, vol. 118, 1–19, doi:10.1002/jgra.50224, 2013.

Muschietti L. and B. Lembège (2017), Two-stream instabilities from the lower-hybrid to the electron cyclotron frequency: application to the front of quasi-perpendicular shocks, Annales Geophysicae, 35, 1093-1112, https://doi.org/10.5194/angeo-35-1093-2017.

Morse, D. L., W. W. Destler, and P. L. Auer (1972), Nonstationary Behavior of Collisionless Shocks, Physical Review Letters 28, 13–16.

Newbury, J.A. and C.T. Russell (1996), Observations of a very thin collisionless shock, Geophys. Res. Lett., 23, 781-784.

Newbury, J. A., C. T. Russell, and M. Gedalin (1998), The ramp widths of high Mach number, quasi-perpendicular collisionless shocks, J. Geophys. Res., 103, 29,581.

Nishimura, K., H. Matsumoto, H. Kojima, and S. P Gary (2003), Particle simulation of re-formation at collisionless perpendicular shocks: Coherent behavior of reflected ions, J. Geophys. Res., 108}(A5), 1182, doi: 10.1029/2002JA009671.

Paul, J.W.M., L.S. Holmes, M.J. Parkinson and J. Sheffield (1965), Experimental observations on structure of collisionless shock waves in a magnetized plasma, Nature, 208, 133.

Paschmann G., N. Sckopke, S.J. Bame, and J.T. Gosling (1982), Observations of gyrating ions in the foot of nearly pependicular shock, Geophys. Res. Lett., 9, 881.

Rème, H., et al. (2001), First multispacecraft ion measurements in and near the Earth's magnetosphere with the identical Cluster ion spectrometry (CIS) experiment, Annales Geophysicae, 19: 1303–1354.

Russell, C.T., and E.W. Greenstadt (1979), Initial ISEE magnetometer results: shock observations, Space Sci. Rev.,23,3.

Russell, C. T., M M. Hoppe, W. A. Livesey, J. T. Gosling, and S. E. Bame,(1982) ISEE 1 and 2 observations of laminar bow shocks' Velocity and thickness, Geophys. Res. Lett., 9 (10), 1171.

Schöler, M., Shinohara, I. and Matsukiyo, S. (2003), Quasi-perpendicular shocks: Length scale of the cross-shock potential, shock reformation, and implication for shock surfing, J. Geophys. Res., 108(A1), 1014.

Schöler, M., and S. Matsukiyo (2004), Nonstationarity of quasi-perpendicular shocks: a particle simulation with different ion to electron mass ratio, Ann. Geophys., 22, 2345.

Schmitz, H. S. C. Chapman and R. O. Dendy (2002), The influence of electron temperature and magnetic field strength on cosmic-ray injection in high Mach number shocks, The Astrophysical Journal, 570:637–646, 2002.

Schwartz, S., M. Thomsen, and J. Gosling (1983), Ions Upstream of the Earth's Bow Shock: A theoretical comparison of alternative source populations, J. Geophys. Res., 88 (A3), 2039.

Schwartz, S., E. Henley, and J. Mitchell (2011), Electron Temperature Gradient Scale at Collisionless Shocks, Phys. Rev. Lett., 107, 215002.

Schwartz, S. (1998), ISSI Scientific reports series 1, 249, http://www.issibern.ch/pdf-Files/analysis_methods_1_1a.pdf.

Sckopke, N., G. Paschmann, S.J. Bame, J.T. Gosling and C.T. Russell (1983), Evolution of ion distribution across the nearly perpendicular bow shock, Specularly and non-specularly reflected-gyrating ions, J. Geophys. Res., 88, 6121.

Scudder, J.D., et al. (1986), The resolved layer of a collisionless high supercritical, quasiperpendicular shock wave.1. Rankine-Hugoniot geometry, currents, and stationarity, J. Geophys. Res., 91, 11,019.

Shinohara, I., M. Fujimoto, R. Takaki, and T. Inari (2007), A 3-D particle-in-cell simulation of quasi-perpendicular shock on Fujitsu fx1 Cluster, Journal of Latex Class fFles, vol. 6, no. 1.

Walker, S. N., Balikhin, M. A. and Nozdrachev, M. N. (1999), Ramp nonstationarity and the generation of whistler waves upstream of a strong quasi-perpendicular shock, Geophys. Res. Lett., 26, 1357.

Walker S.N., H. St. C.K. Alleyne, M.A. Balikhin, M. André and T.S. Horbury (2004), Electric field scales at quasi-perpendicular shocks, Annales Geophys., 1432-0576/ag/2004-22-229.

Winske, D. and Quest, K. B. (1988), Magnetic field and density fluctuations at perpendicular supercritical collisionless shocks,
J. Geophys. Res., 93, 9681.

Woods, L. (1969). On the structure of collisionless magneto|plasma shock waves at supercritical Afvén mach numbers. Journal of Plasma Physics, 3 (3), 435-447.

Woods, L. (1971). On double-structured, perpendicular, magneto-plasma shock waves. Plasma Physics, 13 (4), 289.

Yang, Z.W., Q. M. Lu, B. Lembège, and S. Wang (2009), Shock front nonstationarity and ion acceleration in supercritical perpendicular shocks, J. Geophys. Res., vol. 114, a03111, doi:10.1029/2008ja013785.

Yang Z. W., B. Lembège, and Q.M. Lu (2011), Acceleration of heavy ions by perpendicular collisionless shocks: impact of the shock front nonstationarity, J. Geophys. Res., 116, A10202, doi:10.1029/2011JA016605

Yuan, X., I. H. Cairns, L. Trichtchenko, R. Rankin, and D. W. Danskin (2009), Confirmation of quasi-perpendicular shock reformation in two-dimensional hybrid simulations, Phy. Res. Lett., vol. 36, l05103, doi:10.1029/2008gl036675, 2009.